Physics – Uspekhi **67** (10) 1000 – 1021 (2024)

REVIEWS OF TOPICAL PROBLEMS

PACS numbers: 32.80.Zb, **34.20. – b, 34.35. + a, 34.50. – s,** 34.50.Bw, 34.80.Dp, 52.20.Hv, **61.85. + p,** 68.49.Sf

Stopping and scattering of keV-energy atoms in matter

P Yu Babenko, A N Zinoviev, A P Shergin

DOI: https://doi.org/10.3367/UFNe.2024.03.039666

Contents

Abstract. **Significant progress in understanding the stopping and scattering of atomic particles with energies less than 100 keV in matter is discussed. Stemming from a comparison of experimental data with the results of computer modeling, it refers to the selection of the potential employed to describe the scattering of particles and refinement of the concepts of nuclear and electronic stopping power. Considered is the dominant role in the formation of electronic losses of the mechanism related to the excitation of autoionization states during the rearrangement of molecular shells in collisions. The contribution of fast electron emission to the electronic loss cross section is found to be significant. The influence of collision parameters on scattering, sputtering, and channeling is analyzed.**

Keywords: atomic collisions, atomic interaction potential, nuclear and electronic stopping losses, excitation of autoionization states, ionization of atoms, electron emission, scattering, sputtering, channeling

P Yu Babenko [(a)], **A N Zinoviev** [(b)], **A P Shergin** [(c)]
Ioffe Institute, Russian Academy of Sciences,
ul. Politekhnicheskaya 26, 194021 St. Petersburg, Russian Federation
E-mail: [(a)] babenko@npd.ioffe.ru, [(b)] Zinoviev@inprof.ioffe.ru,
[(c)] A.Shergin@mail.ioffe.ru

Received 15 November 2023, revised 7 March 2024
Uspekhi Fizicheskikh Nauk **194** (10) 1059 – 1081 (2024)
Translated by M Zh Shmatikov

1. Introduction

Collisions of atomic particles (atoms, ions) occur in various laboratory systems and natural phenomena, which necessitates their comprehensive study. Significant advances in modern physics are associated with the study of the interaction of charged-particle beams with solids. It is the charged-particle beams that have proven to be a convenient tool for studying the atomic structure, like Rutherford's experiment, in which a thin metal foil was bombarded with α-particles, which led to the discovery of a heavy nucleus in the center of the atom.

Elementary processes occurring during the collision of atomic particles determine the operating conditions of gas lasers and gas-discharge radiation sources. Collision processes play an important role in the operation of various laboratory installations containing gas or plasma, such as magnetohydrodynamic generators, thermionic converters, plasmatrons and plasma-chemical reactors, and shock tubes.

Elementary processes in collisions of atomic particles also underlie numerous natural phenomena: they determine the properties of the photosphere and the solar corona, various astrophysical phenomena, and the properties of Earth's atmosphere (different elementary processes being significant for different altitudes of the atmosphere). Many natural phenomena, such as magnetic storms and polar lights, are associated with the solar wind, a stream of ionized particles flowing from the solar corona into the surrounding space. Currently, reliable information on the cross sections of various atomic collisions is required in such areas of research as astrophysics, solar physics, and upper atmospheric physics [1].

We list below the main areas of science and technology in which understanding the nature of atomic collisions is of importance.

Ion implantation [2] is used to introduce impurities into semiconductor crystals to manufacture electronic devices. If the introduction dose is large, the surface layer can be transformed into another chemical compound. For a number of metals, ion bombardment can be used to electrochemically passivate a surface. Ion implantation can also be applied to increase the critical temperature of a superconductor, enhance the hardness of metals, manufacture light guides, and conduct research in radiation physics. It is the option of using ion implantation to modify semiconductor materials and metals that has aroused great interest among researchers in this area, which has led to the development of various concepts about the interaction of particles with a solid.

Sputtering of materials during ion bombardment [3–6] is used to clean and etch surfaces, manufacture thin films, and analyze surfaces, and in the operation of sputtering ion sources. An instrumental role in the development of concepts of the interaction of particles with matter was played by the sputtering theory proposed by Sigmund [7]. This work and its modifications enabled development of a reliable theoretical basis for describing practically important sputtering processes.

Studies of the scattering of incident particles by solid targets are of great importance for theory and applications [8–10]. At particle energies ranging from 100 keV to 2 MeV, they are widely used for the analysis of the 500-nm-deep surface layer by Rutherford ion scattering spectroscopy (RBS). At particle energies of ~ 1 keV, slow ion scattering spectroscopy (LEIS) allows studying the composition of the surface monolayer with high sensitivity. Hydrogen scattering plays an important role in hydrogen recycling in thermonuclear facilities.

Atomic and molecular physical processes play a significant role in heating, cooling, losses, diagnostics, and modeling of high-temperature plasma [11, 12]. Sputtering, backscattering, and implantation strongly affect the walls of thermonuclear and plasma installations. An important problem is the damage to structural materials of nuclear reactors due to the action of atomic particles [13, 14]. In a thermonuclear reactor, the first, vacuum wall of the chamber will be exposed to large flows of various types of radiation. The interaction of radiation with wall materials leads to a change in the physical and mechanical properties of the latter and contamination of the plasma with wall materials.

The phenomena that occur during the interaction of particles with solid matter and plasma are widely used in corpuscular diagnostics of laboratory and space plasma. The elemental base of space devices (microcircuits) is exposed to irradiation with heavy charged particles and high-energy protons. Electronics should be developed that will operate sustainably under intense radiation exposure. In medicine, proton therapy uses high-energy proton beams to irradiate diseased tissue, most often in the treatment of cancer [15].

A detailed description of modern concepts of the interaction of atomic particle beams with matter, particle ranges, and the formation of radiation defects can be found in monographs [16–18]. However, this area of research continues to develop intensively, which is due to a lack of understanding of the physics of a number of phenomena and corresponding models, disagreement between the predictions of existing theories and experimental data, and the importance of understanding the physics of phenomena for numerous applications. The achievements of numerous research groups reported at ICACS, ISI, IBA, etc. international conferences contribute to the development of this area of science. In this review, we focus on discussing only that part of these studies that are directly related to the exploration of the stopping and scattering of keV atoms in matter.

The objective of this review is to compare computer simulation data with experiment to verify and refine current concepts of the interaction of atomic particles with energies less than 100 keV with matter. This energy range is selected, since, at high energies, there is good agreement between theory and experiment, and reliable theoretical models are available. At energies below 100 keV, theoretical models of ionization and excitation of particles require the application of strong coupling methods for many states to account for the dynamics of collisions. At the same time, this energy range is of importance for studying collisions in the near-wall region of tokamak reactors and developing low-energy ion implantation methods for miniaturizing electronic devices.

The main factors determining the accuracy of computer modeling are the use of adequate interaction potentials for describing multiple particle scattering and nuclear stopping losses and application of state-of-the-art concepts of electronic stopping losses. It is important to take into account such factors as target structure, thermal vibrations of target atoms, and the presence of a surface potential barrier.

2. Computer modeling methods

Computer modeling methods are described in detail in monograph [18]. The atoms moving in matter lose energy through scattering on the nuclei of target atoms (elastic losses — nuclear stopping power (NSP)) and through excitation and ionization of the electron subsystem (inelastic losses — electronic stopping power (ESP)). Figure 1 presents data on NSP and ESP from the SRIM (Stopping and Range of Ions in Matter) database [19]. As a first approximation, it is assumed that both types of losses are independent of each other and act simultaneously [20]. We discuss this issue in Section 4.

The proposal by Oen and Robinson [21] to use the approximation of successive pair collisions, which enabled modeling the formation of defects in solids under ion

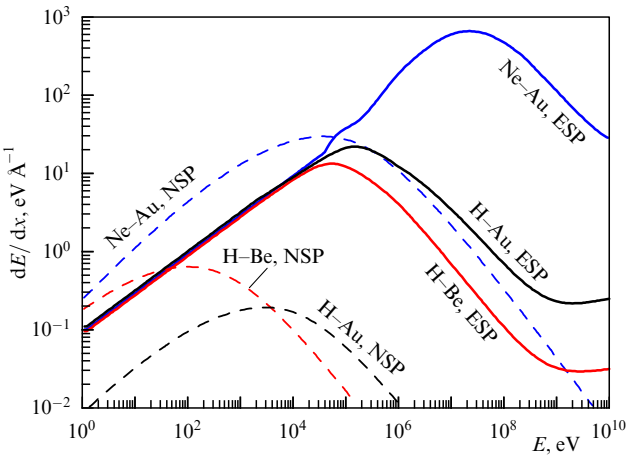

Figure 1. Electronic and nuclear stopping powers for H–Be, H–Au, and Ne–Au systems.

bombardment, made a significant contribution to computer simulation methods. In this approximation, the scattering of atomic particles in a solid is considered a sequence of pair collisions with atoms of the solid. The particle trajectory is replaced by the trajectory asymptotes. At collision energies below 50 eV, the approximation is no longer applicable. The pair collision approximation makes it possible to significantly speed up calculations.

One of the first results of the application of computer methods was the prediction of the channeling effect in crystals, which was later confirmed experimentally.

An important step in the development of the computer modeling method was the work of Ziegler, Biersack, and Littmark on the analysis of ion ranges in solids, which led to the creation of the widely used SRIM code [19]. The application of 'magic' formulas in this code to describe particle scattering yields incorrect results when it is of importance to take into account the scattering of particles at large angles, for example, in describing the spectra of backscattered particles or sputtering of materials by light ions. The specialized codes SDTrimSP (Static and Dynamical TRansport of Ions in Matter for SPuttering) [22] for sputtering and T-RBS (Trim-Rutherford BackScattering) [23] for backscattering have proved their efficiency.

Modern calculations widely use the molecular dynamics method, in which the motion of all interacting atoms is calculated as a function of time. The trajectories of atoms and molecules are determined by numerically solving Newton's equations of motion, where the forces between particles are often calculated using interatomic multiparticle potentials. Calculations based on this model are very computer intensive.

A program code was used in [24, 25] that allowed easily changing the interaction potential, the model of electronic stopping losses, and the target structure; it also enabled taking into account the presence of thermal oscillations, the surface potential barrier, and straggling. In the code's applicability region, the pair collision approximation was used. In computing sputtering, the trajectories of sputtered particles were calculated using multiparticle potentials. In examining channeling, the trajectories of particles were calculated.

3. Interatomic interaction potentials

The results of modeling particle scattering are very sensitive to the choice of the potential model. This problem has been discussed in many publications [7, 8, 18, 26–32]. The first information on the interaction potentials of particles at close approach, when the inner shells of the colliding atomic particles are involved in the interaction, was obtained in the experiments by Everhart et al. [31] using the procedure for processing scattering cross sections [33]. The potential proposed by Firsov [34], based on the statistical theory of the atom, was shown to decrease too slowly with increasing internuclear distance, and screened Coulomb potentials were proposed in its stead.

Study [32] examined the effect of multichannel scattering on the obtained potentials to conclude that the single-channel or 'average' potential model is highly applicable for describing the scattering of particles with energies of 12–300 keV.

Ziegler, Biersack, and Littmark [29] proposed a potential (we refer to it below as 'ZBL potential') obtained by averaging the potential calculations in the statistical model of the atom for a large number of systems. In [30], experimental data on potentials obtained primarily at low collision energies were compared with various theoretical models, and a conclusion was made about the relatively good applicability of the ZBL potential. Nevertheless, even after the appearance of the ZBL potential, the Moliere [35] and Lenz–Jensen [36] potentials and the potential known as Kr–C, proposed in [37], were used with greater or lesser success in many studies.

The behavior of potentials at small internuclear distances was analyzed in [38, 39], where it was shown that, in describing collisions by a screened Coulomb potential $U(R) = Z_1 Z_2 \exp(-\alpha R)/R$, the screening constant α can be calculated using the formula

$$\alpha = -\frac{\left(H_{\rm el}(Z_1+Z_2,0) - H_{\rm el}(Z_1,\infty) - H_{\rm el}(Z_2,\infty)\right)}{Z_1 Z_2}\,, \tag{3.1}$$

where Z_1 and Z_2 are the charges of the nuclei of the colliding atomic particles, R is the internuclear distance, $H_{\rm el}(Z_1+Z_2,0)$ is the energy of the electron subsystem of the united atom, and $H_{\rm el}(Z_1,\infty)$ and $H_{\rm el}(Z_2,\infty)$ are the energies of the electron subsystems of the separated atoms. Using the calculations of [40], the energy of the electron subsystem can be represented as

$$H_{\rm el}(Z) = 0.465 Z^{2.432}\ [\text{at. units}]\,. \tag{3.2}$$

This formula is valid with an accuracy of 1.6% for $Z = 2-92$. The resulting dependence somewhat differs from that predicted by the Thomas–Fermi model of the atom, in which $H_{\rm el}(Z) \sim Z^{7/3}$. Taking into account Eqn (3.1), the following formula is obtained for the screening constant:

$$\alpha = -0.465\,\frac{\left[(Z_1+Z_2)^{2.432} - Z_1^{2.432} - Z_2^{2.432}\right]}{Z_1 Z_2}\,. \tag{3.3}$$

This formula can be approximately represented as

$$\alpha = 2.815\left[1 + 0.022\,(Z_1+Z_2)\right]. \tag{3.4}$$

The formula remains valid to within 3% for systems of atoms with $Z_{1,2} = 5-92$. Since the electron energy of a subsystem decreases in absolute value in the case of excitation or ionization of colliding particles, Eqns (3.3) and (3.4) provide an upper limit on the screening constant. Formula (3.4) is suitable for a rough estimate.

Equations (3.3) and (3.4) for estimating the screening constant, derived from first principles, can be used to adjust the scattering cross section when implementing the Rutherford backscattering method and to estimate corrections associated with electron screening during tunneling in the nuclear fusion cross sections when making measurements on targets containing electrons.

A new attempt to compare theory and experiment was made in [41]. It was shown that the data on the scattering cross sections for various collision energies fits well onto a single universal curve in the reduced coordinates $\rho = \Theta\,{\rm d}\sigma/{\rm d}\Omega \sin\Theta$ and $\tau = E_{\rm cm}\Theta$ ($E_{\rm cm}$ and Θ are the collision energy and the scattering angle in the center-of-mass system). This implies that the scattering is quasi-elastic in nature, and the procedure proposed by Firsov [33] can be used to extract the potential parameters from experiment.

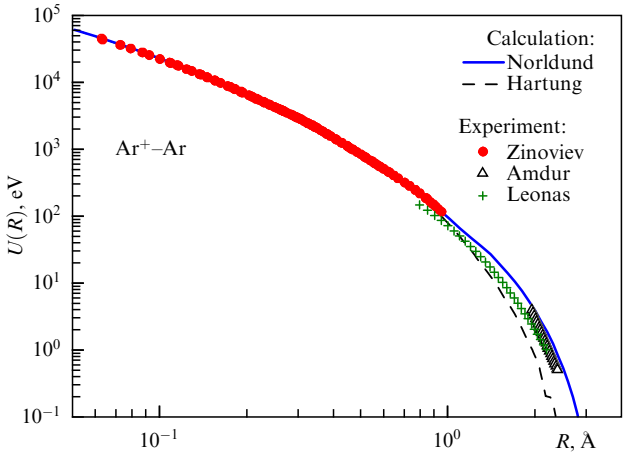

Figure 2. Ar–Ar potential: comparison of calculation and experiment. (Figure taken from [43].)

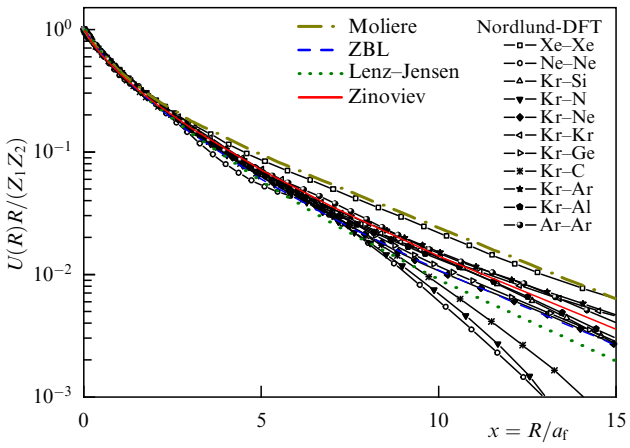

Figure 3. Comparison of calculated DFT potentials with popular theoretical models [43].

The interaction potentials were obtained for 13 systems [41]. The error in the potential value, which is associated with the integration of the dependence of the cross section on the scattering angle, usually does not exceed 3%. The error in the calibration of the R values is associated with the inaccuracy in measuring the absolute values of the cross sections and is estimated by the authors of the study at 4%. For the potential that best describes the experiment, a functional form — the Zinoviev potential — was proposed [41]:

$$U(R) = \frac{Z_1 Z_2 a_f}{x} \exp\left(-\frac{1.575x}{1 + 0.719x^{0.5} - 0.010x}\right), \qquad (3.5)$$

where $x = R/a_f$ and $a_f = 0.8853/(Z_1^{2/3} + Z_2^{2/3})^{1/2}$ is the Firsov screening length [34], expressed in atomic units. It was shown that the universal notation of the potential is only applicable for the region $x < 7$. Equation (3.5) can be used to make a express assessment of the interaction potential.

To obtain more accurate values of the potential for specific pairs, it was proposed in [42] to use the DMol software package with an extended set of wave functions in the density functional approximation (referred to below as Density Functional Theory (DFT)). In [43], the interaction potentials for 19 systems were calculated in the model, and a detailed comparison with the experiment was carried out (Fig. 2). Good agreement with the experiment was achieved.

Figure 3 shows a comparison of the potential calculations for various systems with theoretical models. It can be seen that, to increase the accuracy of the calculations, it is advisable to use an individual potential for a specific system calculated in the density functional approximation. In cases where the potential contains an attractive potential well, it was the proposed in [44] to refine the parameters of the potential well using spectroscopic measurement data [45].

The values of the DFT potentials for various systems can be found in [43, 75], and data on the parameters of the potential well, in monograph [45].

At low collision energies (less than 100 eV), multiparticle potentials should be used and molecular dynamics methods applied.

Examples of multiparticle-potential calculations for Be and W targets are presented in [47–51]. For carbon-containing systems, the Tersoff potential is often used [52]. Studies of multiparticle potentials are reviewed in [52].

4. Universal Lindhard function for describing scattering of atomic particles

Lindhard, Nielsen, and Scharff [54] showed that, for screened Coulomb potentials,

$$U(R) = \frac{Z_1 Z_2 e^2}{R} \Phi\left(\frac{R}{a}\right), \qquad (4.1)$$

where $\Phi(R/a)$ is the screening function, and the scattering cross section of atomic particles, which depends on two variables, the scattering angle θ and the collision energy E, can be described with good accuracy by a function of only one variable $\eta = \varepsilon \sin(\theta/2)$, with

$$\varepsilon = \frac{M_2}{M_1 + M_2} \frac{a}{Z_1 Z_2 e^2} E, \qquad (4.2)$$

where M_1, M_2, Z_1, Z_2 are the masses and charges of the colliding particles, e is the electron charge, and a is the screening length in the potential. In the original work, the variable $t^{1/2} = \eta$ was used.

The scattering cross section in the center-of-mass system $d\sigma/d\Omega$ is related to the function $f(\eta)$, proposed in [54], by the formula

$$\frac{d\sigma}{d\Omega} = \frac{a^2}{8\varepsilon} \frac{f(\eta)}{\sin^3(\theta/2)}. \qquad (4.3)$$

For large values of η, when scattering is described by the Rutherford formula, $f = 1/(2\eta)$.

The function $f(\eta)$ can be used to calculate the cross section of nuclear stopping losses, $S(E)$:

$$S(E) = 4\pi a\, Z_1 Z_2 e^2 \frac{M_1}{M_1 + M_2} s(\varepsilon), \qquad (4.4)$$

where

$$s(\varepsilon) = \frac{1}{\varepsilon} \int_0^{\varepsilon} f(\eta)\, d\eta. \qquad (4.5)$$

In publications, $s(\varepsilon)$ and ε are called Lindhard coordinates. These coordinates are convenient to compare NSP data for various systems.

The function $f(\eta)$ can be analytically described [55]:

$$f(\eta) = A\eta^{1-2m}\left[1 + (2A\eta^{2(1-m)})^{q}\right]^{-1/q}. \quad (4.6)$$

The parameters A, m, q for the Firsov, Bohr, Moliere, and Lenz–Jensen potentials are taken from [18]; for KrC, from [56]; and for the last two cases, calculated by us.

In [57], the fulfillment of the Lindhard approximation for various analytical potentials was verified. For low collision energies, a 10% discrepancy appears at angles of 15–20°. As the energy increases, the curves begin to approach a universal curve and intersect it, and a drop in the cross section sharper than that predicted by the universal curve is observed. With a further increase in the collision energy, the case of a weakly screened Coulomb potential is implemented, and the difference decreases. The Lindhard curve coordinates are chosen in such a way that, in the case of the Coulomb potential, a single curve yields an exact result, in accordance with the Rutherford formula.

In the experiment, the effective scattering cross section is measured, which may include the contribution of inelastic channels. In collisions of keV-range particles, the contribution of inelastic channels leads to the appearance of singularities in the quasielastic scattering cross sections. Figure 4 presents calculations of the Lindhard function for various potentials and a comparison with the experimental data [58–62]. The best agreement with the experiment is provided by the potential proposed by Zinoviev [41]. The curves obtained for the Thomas–Fermi–Firsov and Bohr potentials differ significantly from the experimental data. The spread of the experimental data in the region of the maximum ($\varepsilon = 0.2$) does not exceed ±10%. At high energies, the universal curve describes the experiment fairly well. At $\varepsilon = 0.01$, the scatter of experimental data is ±15%, which is comparable to that of data predicted by various potential models. With a further decrease in the collision energy, the scatter increases significantly.

The scatter of experimental data for various systems is fairly large, which hinders choosing a potential that describes all the studied collision cases. If we fix the case under study, the presence of singularities in the differential scattering cross sections leads to a deviation of up to 15–25%, although the general behavior of the curve can be described quite accurately. As shown in [32], the appearance of singularities is associated with multichannel inelastic scattering. If inner shells are excited, the $Q/U(R_0)$ ratio may be used as a characteristic parameter to estimate the magnitude of the cross section deviation from a smooth curve, where Q is the inelastic energy loss, and $U(R_0)$ is the value of the potential at the trajectory turning point for the angle when a singularity appears in the cross section. Typically, this ratio is 15–20%. This implies that the approximation assuming that NSP and ESP can be considered independently is fulfilled with the same accuracy.

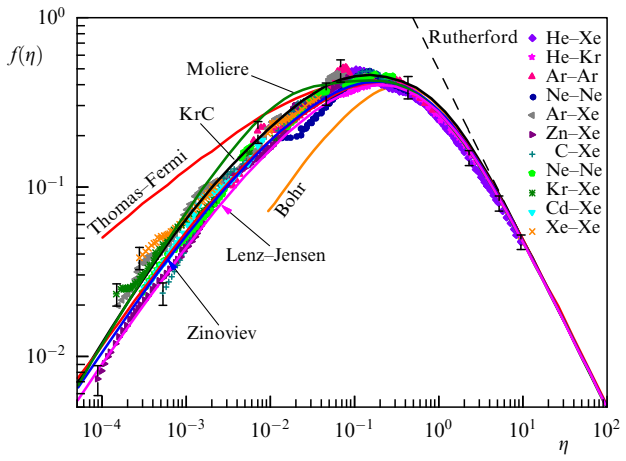

Figure 4. Comparison of universal Lindhard curve for various potentials and measured scattering cross sections. Lindhard screening length was used in processing experimental data.

Table. Parameters used to describe function $f(\eta)$ for various potentials.

Potential	A	m	q
Firsov	1.309	0.333	0.667
Bohr	2.37	0.103	0.570
Moliere	3.07	0.216	0.530
Lenz–Jensen	2.92	0.191	0.512
KrC	3.35	0.233	0.445
ZBL	2.219	0.228	0.577
Zinoviev	2.682	0.213	0.551

It is of importance to take into account the presence of a singularity in the scattering cross section in analyzing the surface layer of a substance, when the main contribution is made by single scattering. The cross section singularities usually arise due to the overlap of the molecular shells of the interacting atoms by 10–15%, so the appearance of singularities upon reaching such internuclear distances can be predicted.

Computer calculations often use the Lindhard approximation, in which nuclear and electronic stopping losses can be taken into account in an additive way. A comparison with the experiment presented in this section shows that the accuracy of this approximation is 15–20%, depending on the range of energies considered. With the specified accuracy, the universal Lindhard curve for a specific potential can be used to calculate the elastic scattering cross section using the parameters displayed in the Table.

5. Screening of particle interactions in metal

The issue of the difference between the potential for particle collisions in a solid and that for collisions in the gas phase is a subject of ongoing discussions.

In modeling the energy spectra of scattered particles in [63], it was noted that, for better agreement with the experiment, the screening constant in the potential should be adjusted. In [25], an analysis of data on rainbow scattering of atoms on the surface of metal crystals yielded interaction potentials that differ greatly from those used to describe scattering in the gas phase. This difference was explained by the influence of the charge induced in the metal by the incident atom [25]. A similar phenomenon was also observed in [64] when describing the scattering of N^{2+} ions on a copper crystal. Unlike the gas phase, it is difficult to determine the potential from the experiment for collisions in a solid due to the influence of multiple scattering and stopping of particles and due to the change in the charge of the particle when passing through the solid.

In [65], the energy and angular spectra of backscattered particles were modeled for proton bombardment of a gold target. Experimental data from [66] were used. The ion–solid interaction potential was shown to differ significantly from the potential describing collisions in the gas phase. The screening constant increased by 10–15%.

This phenomenon was confirmed in modeling the angular distribution of particles when protons pass through a thin gold film [67]. Experimental data from [68, 69] were used. In this case, to describe the experiment, an increase of 15–20% in the screening constant in the potential was needed.

A theoretical description of this phenomenon was reported in [70]. When an ion moves in a solid, the ion potential is screened. The case of collisions with velocities $v < 1$ at. unit, i.e., static screening, was considered.

The interaction potential in the density functional approximation is calculated as the difference in the energy of the system of atoms at a distance of R and $R = \infty$. Discarding the perturbation of the electron density of the system, the potential can be represented as

$$U(R) = \frac{Z_1 Z_2}{R} - Z_1 N_2 \int_0^\infty \int_0^\pi \int_0^{2\pi} \rho(r) \frac{1}{|\mathbf{R} - \mathbf{r}|} r^2 \, dr \, \sin\theta \, d\theta \, d\varphi \,, \tag{5.1}$$

where the first term describes the Coulomb interaction between nuclei, and the second term describes the interaction energy between the charge Z_1 and the electrons of the second particle; N_2 is the number of electrons of the lattice ion. We present $\rho(r)$ in the form proposed in [71]:

$$\rho(r) = \frac{N_2}{4\pi a^2 r} \sum_{i=1}^{3} A_i B_i^2 \exp\left(-B_i \frac{r}{a}\right), \tag{5.2}$$

where A_i and B_i are the expansion coefficients in the Moliere potential [35].

According to [72], the screening constant for an ion with charge Z_2 and number of electrons N_2 can be represented as

$$a = 0.8853 a_B Z_2^{-1.2} N_2^{0.87}, \quad a_B = 0.529 \text{ Å}. \tag{5.3}$$

Substituting $\rho(r)$ in the form (5.2), writing $|\mathbf{R} - \mathbf{r}| = \sqrt{R^2 + r^2 - 2Rr\cos\theta}$, and integrating over θ and φ, we arrive at

$$U(R) = \frac{Z_1 Z_2}{R} - \frac{Z_1 N_2}{2Ra^2} \sum_{i=1}^{3} A_i B_i^2 \times \int_0^\infty dr \exp\left(-B_i \frac{r}{a}\right) \left(R + r - |R - r|\right). \tag{5.4}$$

Separating the integral into two parts, $r < R$ and $r > R$, we obtain

$$U(R) = \frac{Z_1 (Z_2 - N_2)}{R} + \frac{Z_1 N_2}{R} \sum_{i=1}^{3} A_i \exp\left(-B_i \frac{R}{a}\right). \tag{5.5}$$

As a result, a formula was derived similar to that proposed in [72], which describes the interaction between an ion with a charge Z_1 and an ion ($N_2 < Z_2$) or a lattice atom ($N_2 = Z_2$).

In the case of interaction of an ion in a solid, the Coulomb charge of the ion is screened by conduction electrons, and the ion potential can be represented as

$$U_1(R) = \frac{Z_1}{R} \exp\left(-\frac{R}{R_D}\right), \tag{5.6}$$

where R_D is the Debye screening length [73]. For gold, $R_D = 1.358$ at. units. Replacing the Coulomb potential in Eqn (5.1) with the potential of the screened Coulomb charge and performing a similar integration, we obtain the potential of interaction of the ion with the metal lattice screened by conduction electrons:

$$U(R) = \frac{Z_1 (Z_2 - N_2)}{R} \exp\left(-\frac{R}{R_D}\right) + \frac{Z_1 N_2}{R} \sum_{i=1}^{3} A_i \times \exp\left(-B_i \frac{R}{a}\right) \exp\left(-\frac{R}{R_D}\right) \tag{5.7}$$

(see the blue curve in Fig. 5a.)

In the case of a hydrogen atom, the charge of the proton nucleus is screened by a bound electron. For the potential of the hydrogen atom, the formula obtained in [74] is

$$U_2(R) = \left(\frac{1}{R} + \frac{1}{a_B}\right) \exp\left(-\frac{2R}{a_B}\right), \tag{5.8}$$

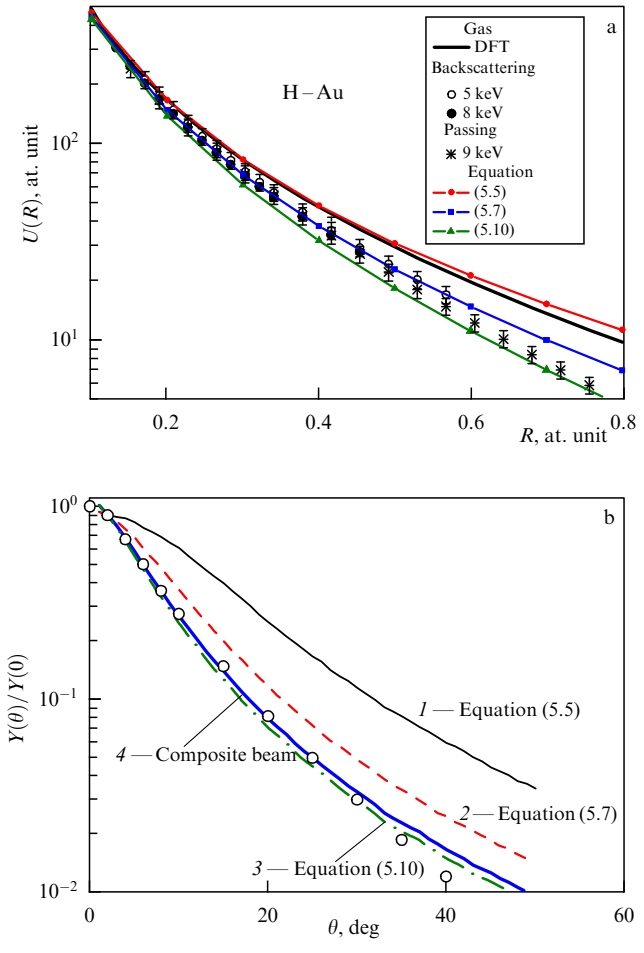

Figure 5. (a) Interatomic interaction potential as a function of distance for case of H–Au. DFT potential for gas phase is displayed. Dots show data from study [65–67], in which potential values were obtained by processing experimental data on particle scattering on the surface or passing through thin films. Lines with dots are calculated using Eqns (5.5), (5.7), and (5.10). (b) Angular distribution of particles that passed through a thin gold film. Dots represent experimental data [68]; measurement errors are ~ 3%. Lines are calculated [70] for potentials (5.5), (5.7), and (5.10). Thick line is calculation for composite beam with neutral atom content of 87.5%.

where the Bohr radius $a_B = 1$ in atomic units. The same result can be obtained if the electron density for the hydrogen atom is represented in Eqn (5.1) as

$$\rho(r) = \frac{1}{\pi a^3} \exp\left(-2\frac{r}{a_B}\right) \tag{5.9}$$

and the corresponding integration over the electron coordinates is carried out.

Replacing the term Z_1/R in the second summand of Eqn (5.5) with $U_2(R)$ and taking into account that $Z_2 = N_2$, we obtain a formula for the interaction potential of a neutral atom with the lattice of a solid:

$$U(R) = \frac{Z_1 Z_2}{R} \sum_{i=1}^{3} A_i \exp\left(-B_i \frac{R}{a}\right) \exp\left(-\frac{2R}{a_B}\right)\left(1 + \frac{R}{a_B}\right). \tag{5.10}$$

Figure 5a displays the dependence of the interatomic interaction potential on the distance between atoms for the H–Au system. The dots show the potential values obtained from an analysis of experimental data on particle backscattering [65] and from experiments on passing through thin films [67]. The solid line is the calculation for the gas phase using the DFT method. Figure 5a shows that the potentials for the gas phase and the solid differ greatly. The red line with circles shows the result of calculations using Eqn (5.5), which virtually coincides with the DFT potential for the gas phase. As can be seen from Fig. 5a, the potentials that take into account the screening describe fairly well the experimental data on the potential for the hydrogen particle in metal.

Figure 5b presents the angular distribution of particles that passed through a thin gold film. The angular distributions obtained for potentials (Eqns (5.5), (5.7), and (5.10)) are also displayed. Potential (5.10) provides good agreement with the experiment. For the case under consideration, 87.5% of the beam are neutral atoms. The calculation for the composite beam completely coincides with the experiment.

The presented formulas (Eqns (5.5), (5.7), and (5.10)) for the potentials can also be used to calculate nuclear stopping losses [70] when protons and hydrogen atoms pass through metals.

Thus, when analyzing the passage of particles in conducting materials, an increase in the screening parameter in the interaction potential should be taken into account.

6. Nuclear stopping losses

As shown below, NSP is completely determined by the interaction potential. In classical mechanics, the scattering cross section is calculated in terms of the dependence of the scattering angle on the impact parameter using a specific interaction potential. The nuclear stopping cross section is expressed by the formula

$$S_n = 8\pi \frac{M_1 M_2}{(M_1 + M_2)^2} E \int_0^\infty \sin^2\left[\frac{\theta(b)}{2}\right] b\, db, \tag{6.1}$$

where M_1 and M_2 are the masses of the colliding particles, $\theta(b)$ is the scattering angle in the center-of-mass system (CMS) at the impact parameter b, and E is the energy of the incident particle.

The nuclear stopping cross section S_n is expressed through the transport cross section Q_{tr} as follows:

$$S_n = Q_{tr} \frac{2M_1 M_2}{(M_1 + M_2)^2} E. \tag{6.2}$$

The quasi-classical approximation does not contain the concept of a trajectory. To calculate the transport cross section in the quasi-classical approximation, the following formula [75] is usually employed:

$$Q_{tr} = \frac{4\pi}{k^2} \sum_{l=0}^{\infty} (l+1) \sin^2(\delta_l - \delta_{l+1}), \tag{6.3}$$

where $k = p/\hbar$ is the wave vector, p is the momentum in the CMS, l is the orbital quantum number, and δ_l is the scattering phase.

The phase δ_l in the quasi-classical approximation is determined by the expression [74]

$$\delta_l = \int_{r_0}^{\infty} \left[\sqrt{2\mu\left[E_{cms} - U(r)\right] - \frac{(l+1/2)^2}{r^2}} - k\right] dr + \frac{\pi}{2}\left(l + \frac{1}{2}\right) - kr_0, \tag{6.4}$$

where r is the internuclear distance, μ is the reduced mass ($\mu = M_1 M_2/\{M_1 + M_2\}$), E_{cms} is the CMS energy, and U is the interatomic interaction potential.

Here, r_0 is the root of the equation:

$$2\mu\left[E_{cms} - U(r_0)\right] - \frac{(l+1/2)^2}{r_0^2} = 0. \tag{6.5}$$

The applicability of the quasi-classical approach to the problem is reduced to the fulfillment of the condition

$$\frac{1}{2\pi}\left|\frac{d\lambda}{dx}\right| \ll 1, \tag{6.6}$$

where $\lambda(x) = 2\pi\hbar/p(x)$ is the de Broglie wavelength of the particle, and x is the coordinate of the particle. Thus, the particle wavelength should change insignificantly over distances on the order of those characteristic of the variation of the potential. In our case, this distance coincides with the size of the potential well $a \sim 1$ Å. The criterion $\lambda/2\pi < 0.1a$ is satisfied for the hydrogen atom up to energies $E > 0.3$ eV.

The conventional criterion for the applicability of the classical description of scattering, $\theta l \gg 1$, in the case of calculating the transport cross section or NSP is reduced to a simpler condition $l \gg 1$, since the main contribution to the NSP cross section is made by angles $\theta \sim 1$.

The formulas presented show that, in calculating both classical trajectories and phases, the choice of potential for an adequate description of the system of interacting particles is of crucial importance.

In [46], NSP calculations were performed for 48 systems using the potential obtained in the DFT approximation with the potential-well parameters adjusted based on the results of spectroscopic measurements.

Figure 6a shows the potentials for the H–C system: the DFT potential and the ZBL potential, which is often used

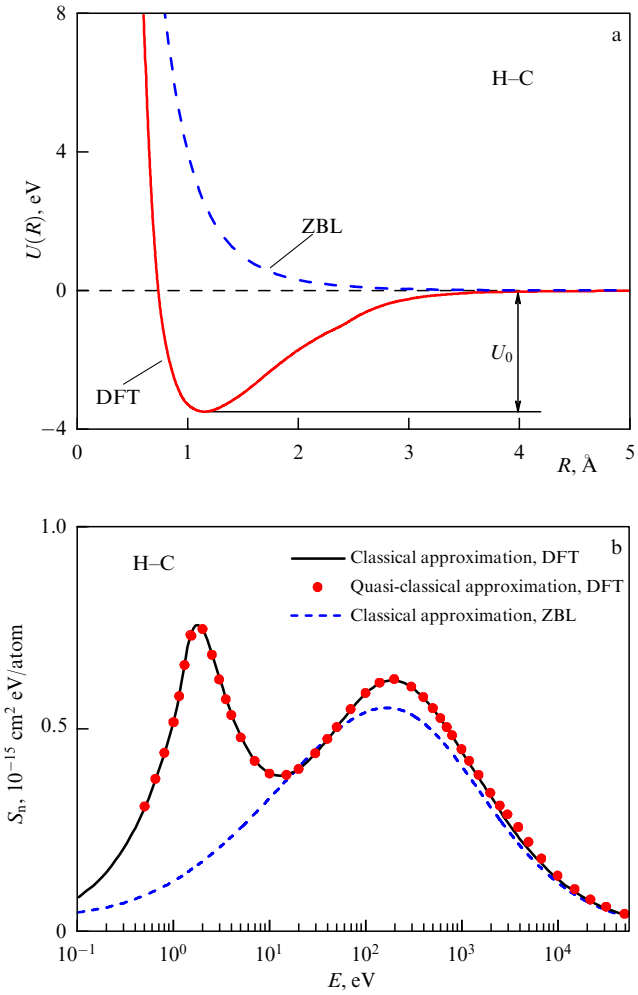

Figure 6. (a) Dependence of interaction potential on interatomic distance for the H–C pair. Dashed line is ZBL potential. Solid line is DFT potential. Well depth in potential is denoted by U_0. (b) Dependence of nuclear stopping cross section on incident particle energy for the H–C pair. Dashed line is 'classical approximation' and ZBL potential; solid line is 'classical approximation' and DFT potential; dots are 'quasi-classical approximation' and DFT potential. (Figures taken from [46].)

in computer modeling programs. It is apparent from the figure that ZBL is a purely repulsive potential. The DFT potential exhibits a potential well with a depth of $U_0 = 3.5$ eV.

Figure 6b shows that, if the nuclear stopping losses are calculated using the ZBL potential, we obtain a dome-shaped curve (dashed line). If a potential with a well is used in the calculation, an additional peak arises due to the strong scattering of atoms by the potential well. This implies that, if we are interested in the values of nuclear losses for low energies of colliding particles, the universal ZBL potential without a well cannot be used.

The calculation yields the same values of energy losses in both the classical and quasi-classical cases, provided the condition $l \gg 1$ is fulfilled.

The presence of an additional peak in the NSP cross sections must be taken into account for collision energies of less than 100 eV; this is especially important when calculating the trajectories of recoil particles in the process of sputtering.

7. Mechanism of inelastic losses associated with promotion of molecular orbitals during particle collisions and formation of autoionization states

Stopping at high collision energies, which was first considered by Bethe [76], is described by the formula

$$S_e = \frac{4\pi Z_1^2 Z_2 e^4}{mv^2} \ln \frac{2mv^2}{I}, \tag{7.1}$$

where v is the velocity, Z_1 is the atomic number of the incident particle, Z_2 is the atomic number of the target substance, and I is a value on the order of the ionization energy (m is the electron mass). In this region, the stopping cross section decreases with increasing energy of the incident particle. Bloch [77] introduced relativistic corrections into this formula, which are insignificant at collision energies of less than 1 MeV.

In the low-energy region, Fermi and Teller [78] investigated electronic stopping in metals, considering the electrons of the metal to be a free degenerate Fermi gas. The Fermi–Teller formula can be represented as

$$S_e = \gamma_F \frac{e^2 a_0}{v_0} v, \quad \gamma_F = 4\pi \frac{a^2}{a_0^2} \frac{v_F}{v_0} Z_2^*, \tag{7.2}$$

where $v_0 = e^2/\hbar$ and $a_0 = \hbar/(mv_0)$ are the Bohr velocity and radius, v_F is the Fermi velocity, Z_2^* is the number of conduction electrons per atom of the target substance, and $a^2 \sim (e^2/mv_F^2)^2$. Equation (7.2) describes the contribution of metal conduction electrons to the stopping; it is applicable provided $v \ll v_F$.

Later, Lindhard and Scharff [20] derived the following formula for the inelastic stopping cross section:

$$S_e = 8\pi e^2 a_0 \frac{Z_1^{7/6} Z_2}{(Z_1^{2/3} + Z_2^{2/3})^{3/2}} \frac{v}{v_0} = Cv. \tag{7.3}$$

The derivation of this formula uses an expression for the permittivity with parameters fitted to the experimental data. Equation (7.3) is valid for velocities $v < Z_1^{2/3} v_0$. To take into account Z_2 oscillations in the inelastic stopping cross sections, an adjustable parameter c_k ranging from 0.67 to 2.4 is often introduced [79–81].

Firsov [82] proposed a model according to which the electron clouds of colliding atoms overlap. By studying the momentum transfer during a collision, it is possible to determine the electronic energy loss. Using the Thomas–Fermi approximation in combination with the momentum approximation of nuclear motion, Firsov derived the following formula for the inelastic energy loss $\mathcal{E}$ [eV]:

$$\mathcal{E} = \frac{(Z_1 + Z_2)^{5/3} 4.3 \times 10^{-8} v}{\left[1 + 3.1(Z_1 + Z_2)^{1/3} 10^7 R_0(p)\right]^5}, \tag{7.4}$$

where v is the velocity of the incident particle expressed in cm s^{-1}, the closest approach distance R_0 is measured in centimeters, and p is the impact parameter. For the stopping cross section S_e, we obtain the formula

$$S_e = 2\pi \int_0^{p_{max}} p\mathcal{E}(p, v)\, dp, \tag{7.5}$$

where p_{max} is the average distance between target atoms.

Both Lindhard's and Firsov's models predict that the stopping cross section is proportional to the velocity. Since the Thomas–Fermi approximation is used to describe electronic shells, it is advisable to use the Firsov model for collisions of heavy atoms. Oen and Robinson [83] proposed a modification of the Firsov model for collisions involving light ions. Review [84] considers other modifications of the Lindhard and Firsov models and frequently used empirical formulas.

It should be noted that Lindhard's and Firsov's models do not take into account the shell structure of atoms, and most other proposed models do not consider the rearrangement of the electronic shells of atoms during collisions.

The current state of research on the theory of particle stopping is reviewed in [85, 86]. Typically, the theory satisfactorily describes losses at high particle energies and near the maximum of the stopping cross section.

In the SRIM code, it is usually assumed at low energies that the ESP is proportional to the collision velocity with normalization to the experimental results in the region of the maximum. Data on the low energies of ion collisions with a solid are less reliable and in many cases are lacking. They are especially necessary in solving the problem of damage to the first wall and divertor of a tokamak reactor and in developing ion implantation methods for ion energies below 10 keV, aimed at miniaturizing the manufactured nanostructures.

It was hypothesized in [87, 88] that the formation of autoionization states during collisions of atoms is the main mechanism of ionization and inelastic energy losses at a collision energy of less than 100 keV. An attempt to take into account the excitation of autoionization states was also made in [89].

We now consider the basic formulas of the proposed model. The contribution of the formation of autoionization states to the electronic stopping power $\mathrm{d}E/\mathrm{d}x$ can be described as

$$\frac{\mathrm{d}E}{\mathrm{d}x} = \frac{2\pi}{V_0}\int Q\left[R_0(b)\right] b\,\mathrm{d}b \approx \frac{2\pi}{V_0}\sum_{nlj}\int Q_{nlj} W_{nlj}(R_0) b\,\mathrm{d}b$$
$$= \frac{2\pi}{V_0}\sum_{nlj} Q_{nlj}^{\mathrm{aver}}\int W_{nlj}(R_0) b\,\mathrm{d}b\,. \qquad (7.6)$$

$Q[R_0(b)]$ is the total value of inelastic energy losses depending on the distance of closest approach R_0. Here, Q_{nlj} are the energies of autoionization states, $W_{nlj}(R_0)$ are the probabilities of excitation of autoionization states depending on R_0, and V_0 is the volume of a single atom in a solid target; the summation is carried out over all promoted states with quantum numbers n, l, and j, and b is the impact parameter. Removing the parameter Q_{nlj} from under the integral does not compromise the generality of the formula if Q_{nlj}^{aver} is understood as the value averaged over the range of parameters b.

It should be noted that the partial cross section for the formation of an autoionization state is

$$\sigma_{nlj}^{\mathrm{a}} = 2\pi\int W_{nlj}(R_0) b\,\mathrm{d}b\,. \qquad (7.7)$$

The decay of an autoionization state leads to ionization with the removal of N electrons; therefore, instead of the cross section for the formation of an autoionization state, $N\sigma_{nlj}^{\mathrm{ion}}$ can be used, where $\sigma_{nlj}^{\mathrm{ion}}$ is the ionization cross section,

$$\frac{\mathrm{d}E}{\mathrm{d}x} = \frac{1}{V_0}\sum_{nlj} N Q_{nlj}^{\mathrm{aver}}\sigma_{nlj}^{\mathrm{ion}}\,. \qquad (7.8)$$

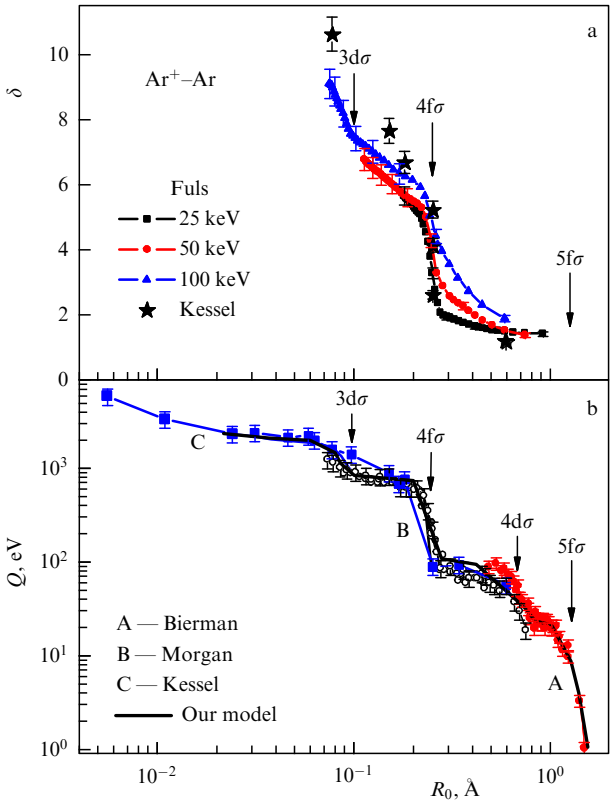

Figure 7. Number of emitted electrons δ (a) and inelastic energy losses (b) for $Ar^+ - Ar$ system as functions of closest approach distance. Arrows indicate thresholds for the promotion of various orbitals. (a) Curves with dots represent data from [90]. Asterisks are coincidence measurements [91]. (b) Data from Bierman [92], Morgan [93], and Kessel [91, 94]. Thick solid line is the model under discussion. (Figure taken from [95].)

The electronic stopping power can be estimated using the ionization cross section and the values of inelastic energy losses for the channels under consideration.

As an example, we consider the case of an Ar–Ar collision.

Figure 7 shows that $Ar^+ - Ar$ collisions feature a correlation between the observed number of emitted electrons and inelastic losses. A sharp increase in both quantities is seen upon reaching those internuclear distances at which the corresponding MO is promoted, and electronic shells are rearranged. At large internuclear distances, $R_0 \approx 1.4$ at. units, excitation of the M shells occurs. At $R_0 \approx 0.22$ at. units, due to the promotion of the $4f\sigma$ orbital in the $L_{2,3}$ shell of Ar, two vacancies emerge; when the promotion of the $3d\sigma$ orbital occurs, two more L vacancies appear.

We now give an example of calculating the stopping cross section for this case. Data on the ionization cross sections of the M shell of Ar can be taken from [96–98]. Data on the excitation cross section of the L shell were obtained in [99]. Using experimental data on inelastic energy losses [92] and the energies of vacancy formation in the $L_{2,3}$ shell of Ar, $\mathrm{d}E/\mathrm{d}x$ can be calculated using Eqn (7.8) (Fig. 8). Figure 8a shows that excitation of the L shell doubles the value of $\mathrm{d}E/\mathrm{d}x$. The proposed model yields values significantly exceeding the SRIM data and predicts a threshold dependence of $\mathrm{d}E/\mathrm{d}x$ on the collision energy.

If measurements of ionization cross sections are unavailable, we recommend using the scaling for the excitation of the L and M shells proposed in [88, 103]. The probability of the formation of an L vacancy upon reaching the internuclear

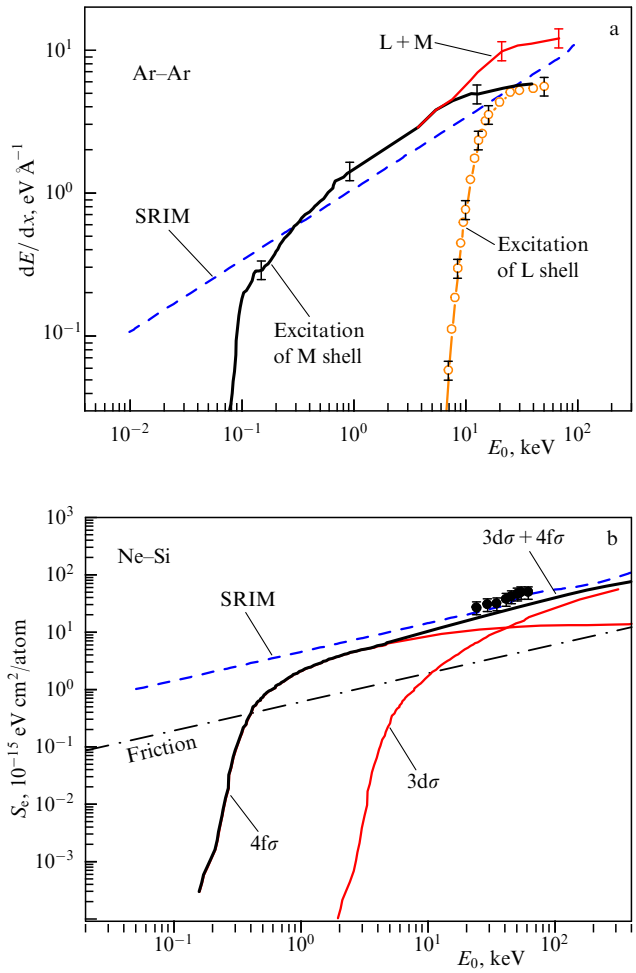

Figure 8. (a) Electronic stopping power in Ar collisions with solid Ar. Thick black line is estimate obtained using ionization cross section [96, 98]. Contribution of L-shell ionization is shown by circles [99]. Thick solid red line is the sum of contributions of L- and M-shell excitation. Dashed blue line is the SRIM calculation. (b) Dependence of electronic stopping cross section for the Ne–Si case on collision energy. Points represent experimental data [101]; dashed line is SRIM data [19]. Contributions from promotion of 3dσ- and 4dσ-orbitals are shown by thin solid lines; dashed-dotted line shows estimated contribution from stopping on conduction electrons, and thick solid line is the summary curve. (Figures taken from [102].)

distance R_0 can be described by the formula

$$W(R_0) = \frac{1}{\beta + \exp\left[\gamma(R_0/R_\mathrm{b} - 1)\right]}\,, \tag{7.9}$$

where $\beta = 1.02$, $\gamma = 22.8$, and the parameter R_b, which is determined from the condition $W(R_\mathrm{b}) = 0.5$, is equal to the internuclear distance R_c at which the 4 fσ orbital intersects the unfilled upper levels. The dependence of R_c on the charges of the interacting particles was obtained in [103] by processing data on the thresholds of excitation of the $L_{2,3}$ shell in collisions of atomic particles in both the gas and solid phases. The ionization cross section associated with the excitation of the $L_{2,3}$ shell is calculated by integrating $W[R_0(b)]$ over all impact parameters:

$$\sigma(E_0) = 2\pi N \int_0^\infty W\left[R_0(b)\right] b\,\mathrm{d}b\,, \tag{7.10}$$

where N is the number of vacancies formed at small R_0.

Figure 8b presents an example of Ne–Si collisions. In this case, the ionization cross sections of the L and M shells were obtained using scaling. It is necessary to take into account the contribution to the stopping losses from the interaction of the incident particle with conduction electrons ('Friction' curve in Fig. 8b). This contribution was estimated using the formulas presented in [100]. As can be seen from Fig. 8b, the obtained data are in good agreement with the experiment [101]. The contribution to the stopping losses from the interaction with conduction electrons is ~ 13%.

When K-vacancies are excited, two fundamentally different cases occur:

(1) In the presence of a vacancy in the 2pπ orbital before the collision, a K-vacancy is formed as a result of rotational transitions within the limits of the combined atom from the 2pσ to the 2pπ orbital.

Based on the studies by Briggs and Macek [104], a scaling (Fig. 9a) can be proposed for the cross section of K-vacancy formation [105]:

$$\sigma_\mathrm{bak}(E_\mathrm{cms}) = f\pi R_\mathrm{2p}^2\, F\left(\frac{E_\mathrm{cms}}{(Z_1 + Z_2 - \delta)^2}\right), \tag{7.11}$$

where E_cms is the collision energy in the center-of-mass system, R_2p is the radius of the 2p shell of the combined atom, $R_\mathrm{2p} \sim (Z_1 + Z_2 - \delta)^{-1}$, Z_1 and Z_2 are the charges of the nuclei of the colliding atoms, and $\delta = 4$ is the correction for the screening of the 2p shell by the electrons of the 1s and 2s shells of the combined atom. The cross section is proportional to the factor f, reflecting the probability of the availability of a vacancy in the 2pπ orbital, which is formed from the 2p shell of the collision partner with a larger Z. In comparison with previously proposed scaling factors, a dynamic correction for the probability of vacancy formation in the 2pπ orbital during a collision is taken into account. The logarithm of the function F is given by the formula $\lg F = -15.767 - 4.493\exp(-x/0.069) - 1.128\exp(-x/1.564) - 8.522\exp(-x/0.026)$, where $x = E_\mathrm{cms}/(Z_1+Z_2-\delta)^2$ [105]. The proposed scaling makes it possible to estimate the ionization cross sections of the K shells for unexplored cases.

It should also be kept in mind that a K-vacancy formed in a light collision partner can pass to the K-shell of a heavier partner due to the dynamic coupling of 2pσ and 1sσ states, the so-called vacancy sharing mechanism. The probability of this process can be estimated using the formulas proposed in [106].

(2) In collisions of atoms and ions with $Z > 10$, the 2pπ orbital is filled, and no transitions from the 2pσ to the 2pπ orbital are possible. Numerous attempts have been made to propose empirical scaling for the formation of K-vacancies for this case [107–109]. However, the authors themselves pointed out that a theoretical explanation for this phenomenon is missing.

The behavior of quasi-molecule terms in the complex plane of internuclear distances was studied in [110]. The existence of branching points linking different terms was discovered. The probability of an electron transition to the continuum is calculated in this theory as an integral encircling the branching points. A formula for the cross section of the emission of an electron with energy E was obtained in this theory in [111]:

$$\sigma(E) = \frac{4\pi\left|R(E)\right|^2 \operatorname{Im} R(E)}{\alpha(E)} \exp\left(-\frac{\alpha(E)}{v}\right),$$
$$\alpha(E) = 2\int_{E_0}^{E} \operatorname{Im} R(\varepsilon)\,\mathrm{d}\varepsilon\,, \tag{7.12}$$

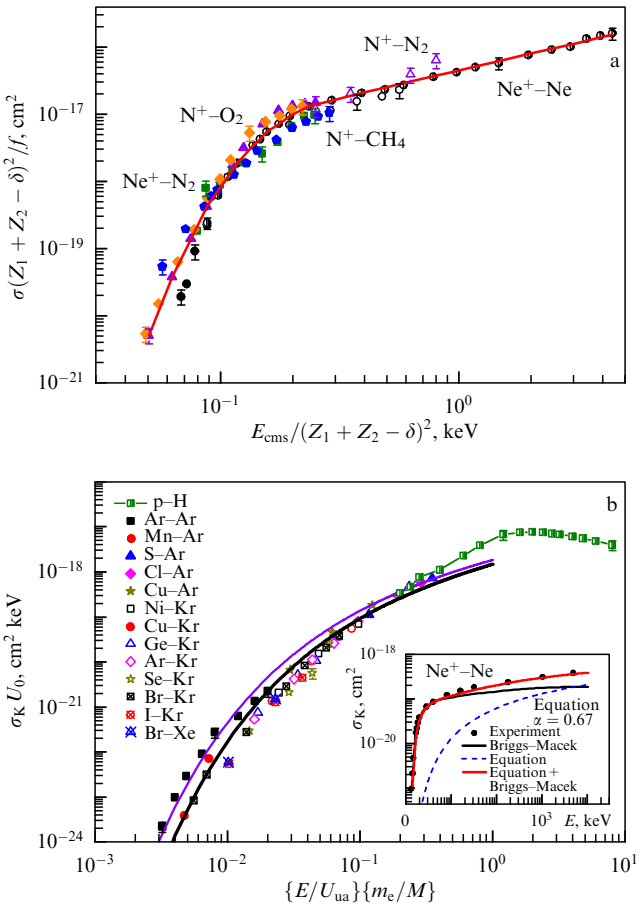

Figure 9. (a) Scaling for cross sections for formation of K vacancies in collisions of light atoms with $Z \leqslant 10$ in the presence of a vacancy in the 2pπ orbital. Dots show experimental data from Meskhi [99], Stolterfocht [113], and Avakyan [14]. Thick line is universal curve proposed in [105]. (b) Scaling for cross sections for formation of K vacancies in collisions of atoms with $Z > 10$ when 2p shell is completely filled and a vacancy is formed due to ionization of 2pσ as a result of collision dynamics. Experimental data are presented for various combinations of colliding atoms from Lennard [107] and for p–H collisions from [14]. Due to difference in the initial population of the 2pσ level, ionization cross section in the p–H case is multiplied by 4. Thin solid line shows curve for the case $\alpha(0) = 0.67$. Thick solid line represents the case $\alpha(0) = 0.75$, which best describes the experiment. Inset to the figure shows contribution of mechanisms under consideration to formation of K vacancies in $Ne^+ - Ne$ collisions. As can be seen, overall curve agrees well with the experiment [113]. (Figure taken from [105].)

where $R(E)$ is the inverse function of the dependence of the term $E(R)$ under consideration on the internuclear distance R, v is the collision velocity, and $\mathrm{Im}\, R(E)$ is the imaginary part of the dependence $R(E)$.

We integrate this expression over the energies of the emitted electron to find the ionization cross section σ_i of the term under consideration:

$$\sigma_i = \int_0^\infty \sigma(\varepsilon)\,\mathrm{d}\varepsilon = \int_0^\infty \frac{4\pi\left|R(E)\right|^2 \mathrm{Im}\, R(E)}{\alpha(E)} \exp\left(-\frac{\alpha(E)}{v}\right)\mathrm{d}E\,.$$

Taking into account that $2\mathrm{Im}\, R(E)\,\mathrm{d}E = \mathrm{d}\alpha$, we can change the integration variable:

$$\sigma_i = \int_{\alpha(0)}^\infty 2\pi\left|R\left[E(\alpha)\right]\right|^2 \frac{v}{\alpha} \exp\left(-\frac{\alpha}{v}\right)\mathrm{d}\alpha\,.$$

The integral is approximately calculated by the saddle-point method:

$$\sigma_i = 2\pi R_0^2 \frac{v}{\alpha(0)} \exp\left(-\frac{\alpha(0)}{v}\right). \tag{7.13}$$

We introduce the dependence of the term on the internuclear distance R:

$$E = -U_0\left[1 + \left(\frac{R}{R_0}\right)^m\right].$$

We obtain then $\alpha(0) \approx 2(m/(m+1))U_0\,\mathrm{Im}\, R_0$. Let us consider the ionization of the 2pσ term in p–H collisions; in this case, $m = 2$ and $U_0 = 0.5$ at. units is the energy of the term in the limit of a united atom. The position of the point of quasi-intersection of the 2pσ term with the continuum was calculated in [112], with $\mathrm{Im}\, R_0(\mathrm{p-H}) = 1.01$. Thus, for the p–H system, $\alpha(0) \approx 0.67$. It should also be taken into account that, in the case of p–H, the 2pσ orbital is filled with a probability of 50%.

In collisions of complex atoms, the 2pσ orbital contains two electrons ($P = 2$). In the limit of a united atom, the level energy $U_0 = 0.5Z_{\mathrm{eff}}^2/n^2$, where Z_{eff} is the effective charge for the level under consideration, $n = 2$ is the principal quantum number, and $R_0 = n/Z_{\mathrm{eff}}$; thus, $Z_{\mathrm{eff}} = (8U_0)^{0.5}$, $R_0^2 = 0.5/U_0$. The position of the quasi-intersection point scales with variation in Z_{eff}:

$$\mathrm{Im}\, R_0(Z_{\mathrm{eff}}) = \mathrm{Im}\, R_0\,(\mathrm{p-H})\,\frac{2}{Z_{\mathrm{eff}}}\,.$$

Consequently,

$$\alpha(Z_{\mathrm{eff}}) = \frac{m}{m+1}\,\mathrm{Im}\, R_0\,(\mathrm{p-H})\,\frac{4}{Z_{\mathrm{eff}}}\,U_0 \approx \alpha(0)\,(2U_0)^{0.5}\,, \tag{7.14}$$

or

$$U_0 \approx \frac{1}{2}\left[\frac{\alpha(Z_{\mathrm{eff}})}{\alpha(0)}\right]^2.$$

For the cross section of 2pσ ionization, we obtain the formula (in atomic units)

$$\sigma_i = \pi P \frac{v}{\alpha(Z_{\mathrm{eff}})U_0} \exp\left(-\frac{\alpha(Z_{\mathrm{eff}})}{v}\right), \tag{7.15}$$

where P is the number of electrons at the 2pσ level.

For comparison with the experiment, it is convenient to introduce the variable x:

$$x = \frac{m_e}{M}\,\frac{E}{U_0}\,,$$

where m_e/M is the ratio of the electron mass to the mass of the incident particle and E is the collision energy.

It can be seen that

$$\frac{\alpha(Z_{\mathrm{eff}})}{v} = \frac{\alpha(0)}{\sqrt{x}}\,,$$

and the formula for the cross section can be represented as

$$\sigma_i[\mathrm{cm}^2]\;U_0\,[\mathrm{keV}] = K\,\frac{\sqrt{x}}{\alpha(0)} \exp\left(-\frac{\alpha(0)}{x}\right), \tag{7.16}$$

where the constant $K = 1.196 \times 10^{-18}$ cm^2 keV.

Figure 9b displays the dependence of the reduced cross section on the reduced energy for various experimentally studied combinations of colliding particles. It can be seen that in these coordinates the experimental points for most cases lie on a common curve. This dependence is well described by Eqn (7.16). The best agreement with the experiment is achieved at $\alpha(0) = 0.75$ and $m = 3$. The same figure shows the ionization cross section for p–H collisions multiplied by 4. It can be seen that this dependence also agrees very well with the first group of experimental data and Eqn (7.16). The applicability of the proposed formula is limited to the $x < 1$ range.

It is interesting to compare two possible mechanisms of K-vacancy formation. As can be seen from the inset in Fig. 9b, the calculation of the K-vacancy formation cross section in the $Ne^+ - Ne$ system carried out in [104] at energies above 200 keV gives cross section values lower than the experiment [113]. Accounting for the correction for ionization of the $2p\sigma$ orbital due to transitions to the continuum using Eqn (7.16) yields almost complete agreement with the experiment.

At low collision energies, the mechanism associated with transitions between orbitals leads to significantly larger cross sections for the formation of K-vacancies than those for the formation of vacancies due to dynamic ionization, and, at high energies, both mechanisms must be taken into account. A distinction must be made between collisions of atoms in the gas and solid phases. In collisions in the solid phase, a cascade of collisions occurs, and additional vacancies can be formed in the outer shells, which can survive until the next collision and lead to larger cross sections for the formation of K-vacancies due to the allowed $2p\sigma$–$2p\pi$ transitions.

It can be expected that the scaling proposed for the cross sections for the formation of K-vacancies in the shells of colliding atoms will be used in calculating the electronic stopping losses during ion irradiation of solids.

Thus, the formation of autoionization states due to the rearrangement of the shells of colliding particles makes a dominant contribution to the ESP at collision energies of less than 100 keV.

8. Contribution of elementary processes and fast electron emission to electronic stopping powers

Studies [114, 115] compared the contribution of elementary processes of ionization, excitation, and charge exchange in p–He and p–Ar collisions to the cross sections of electronic stopping losses. These cases were chosen as the most studied experimentally. In monograph [14], measurement errors were analyzed in detail and recommended values were indicated. A large amount of data is also available in the ALADDIN database [116]. Data on electron energy losses are collected in the NDS database [117]. The cross sections of elementary processes and electronic stopping cross sections were measured by independent authors. As already mentioned, one of the objectives of this review is to compare them and clarify the contribution of various processes to the electronic stopping cross section. To the best of the authors' knowledge, such a comparison based on experimental data has not been carried out before.

Cross sections of electronic stopping loss were calculated in numerous theoretical studies. For the systems we have chosen, reference should be made to [118–120]. Detailed information on studies of electronic stopping losses can be found in reviews [85, 86]. Ionization and spectra of electrons in particle collisions for simple systems are still being studied [121–128].

Theoretical considerations show that the particle ionization process is expected to dominate at high collision energies. An interesting issue is the role of the kinetic energy carried away by the ejected electrons and the description of this process.

We now consider the contribution of the elementary processes of ionization, excitation, and charge exchange to the electronic stopping cross sections in collisions of atomic particles.

The relationship between the electronic stopping cross section S_e and the cross sections of the elementary processes can be set as

$$S_e = \sum_n \left[\sigma_i^n \left(\sum_{n'=1,2,3,\ldots} I_{n'} + nW_e \right) \right] + \sigma_{ex} I_{ex} + \sigma_{cx} \left(\Delta E_{cx} + \frac{m_e}{m_p} E \right), \quad (8.1)$$

where σ_i^n is the cross section of n-fold ionization, I_n is the corresponding ionization potential, and W_e is the average energy carried away by an electron. The second term contains the total excitation cross section σ_{ex} and the transition energy I_{ex}. The third term represents the contribution of charge exchange processes (σ_{cx} is the charge exchange cross section, ΔE_{cx} is the energy difference between the levels during the transition of an electron in charge exchange). According to [129], if the contribution of charge exchange to electronic stopping is taken into account, the term $(m_e/m_p)E$ should be added to the energy difference between the levels of the initial and final states (here, m_e and m_p are the masses of the electron and proton, E is the collision energy), which is related to the transfer of momentum by the electron during the transition from the coordinate system of the target atom to that linked to the fast particle.

Figures 10a and 10b illustrate a comparison of the contributions of various elementary processes to the cross section of electronic stopping losses.

Figure 10 shows that at low energies the main contribution to the cross section of electronic stopping is made by 'H_0-ionization,' while, with increasing energy, ionization by protons dominates. The dashed line in Fig. 10 presents the total cross section of elementary processes without taking into account the contribution of the kinetic energy of emitted electrons W_e. The solid line represents the sum of the cross sections of elementary processes taking into account W_e. In this case, good agreement is achieved between the sum of the contributions of elementary processes and the measurements of electronic stopping losses.

Figure 11 displays the average energy of emitted electrons as a function of the collision velocity. As can be seen from Fig. 11, the average energy first increases and then varies insignificantly. The data obtained from measurements of electronic spectra [130, 131] for the cases under consideration and the values of W_e obtained using Eqn (8.1) are in good agreement.

In the framework of the theory of dynamic ionization, in [111], expression (7.12) was proposed for the cross section of electron emission with energy E.

We use this formula and estimate the average kinetic energy of ejected electrons:

$$W_e = \frac{\int_0^\infty E\,\sigma(E)\,dE}{\int_0^\infty \sigma(E)\,dE}. \quad (8.2)$$

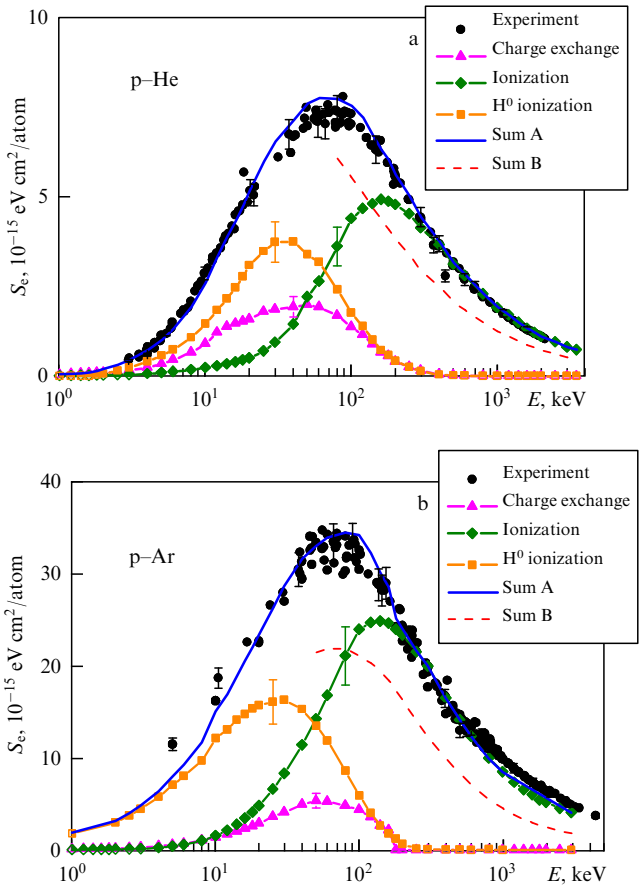

Figure 10. Comparison of contributions of various processes to stopping loss cross section for (a) p–He and (b) p–Ar collisions. Solid line represents sum of all processes taking into account kinetic energy of electrons (Sum A); dotted line is the same, without taking into account contribution of energies of fast electrons (Sum B) [115].

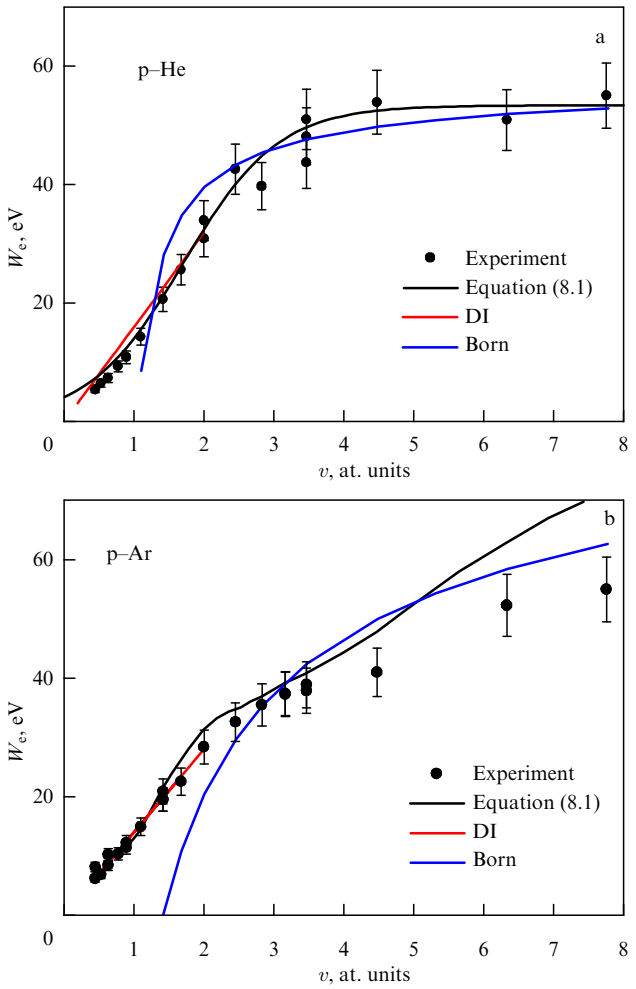

Figure 11. Comparison of experimental dependence of average electron energy with various theoretical models. Predictions of dynamic ionization theory (DI) and Born approximation are also displayed. (Figure taken from [115].)

Having estimated the integrals using the saddle-point method, we obtain a simple formula for W_e [115]:

$$W_e \approx \frac{v}{2\,\mathrm{Im}\,R_0}\,. \tag{8.3}$$

The resulting formula (8.3) predicts that the average energy of the ejected electron is proportional to the collision velocity, which is confirmed experimentally (see Fig. 2) at collision energies $v < 2$ at. units.

At high collision energies (in the Born approximation), the parameter W_e can be estimated using the formula

$$W_e = \frac{S_e - \sigma_{ex} I_{ex}}{\sigma_i} - I\,. \tag{8.4}$$

The quantities used are described in Eqn (8.1).

The Born approximation predicts the independence of W_e from the collision velocity at high energies. As shown in Fig. 11, the obtained velocity dependence of the average electron energy is well described in various velocity ranges by the models under consideration.

Thus, quantitative agreement between the cross section of the stopping losses and the sum of the contributions of ionization, excitation, and charge exchange can be achieved if we take into account the significant energy losses due to fast knocked-out electrons. At high collision energies, up to 70% of the total stopping losses are associated with electron kinetic energy. To estimate the electron energy at $v < 2$ at. units in the dynamic ionization approximation, a formula has been proposed that describes the experimental data well; at high energies, it is recommended to use the Born approximation.

9. Effect of multiple collisions on electronic stopping powers

To describe the physical processes occurring in a solid bombarded with atomic particles, it is necessary to know the value of electronic stopping powers for a large set of cases. A database of electronic stopping powers NDS is available, which includes a set of experimental data and the results of computer modeling of electronic (inelastic) energy losses of atomic particles in matter [117].

For the experimental determination of electronic stopping losses, two types of geometry are used: the reflection of a particle beam from the surface of a massive target and the passage of a beam through thin films.

In the reflection configuration, the energy spectrum of scattered particles is measured, and the shape of the spectrum is modeled by a computer code in which the fitting parameter is the value of the electronic stopping losses.

In the passing configuration, the energy spectrum of scattered particles is also measured. The 'shift' of the spectrum along the energy scale gives the average loss of particles after passing through the film. Then, the value of the energy loss is divided by the film thickness, yielding as a result the energy loss per unit length.

As was shown by Moro [132], at energies above 10 keV, the data obtained by both methods agree within the experimental errors. However, at lower energies, for many combinations under bombardment with Si, Ni, Cu, Zn, Ag, and Au protons [133–149], the absolute values of the losses differ by a factor of 2 to 3.

The reasons for the disagreement among the results obtained by different methods have been widely discussed at specialized international conferences and in a number of publications [150–152]. In particular, Paul [150] analyzed in detail possible errors in measurements and the effect of differences in angular distributions for backscattered particles and particles that have passed through thin films, but no explanation of the differences in the obtained values of electronic stopping loss has been suggested. Sigmund [151] attributed this difference to the dependence of the inelastic loss on the impact parameter. Of course, such a dependence can exist, but as numerous experiments carried out in the gas phase show, the inelastic energy loss increases with a decrease in the impact parameter, whereas, in the method of detecting backscattered particles, the measured value is usually smaller than that measured by the method of passing through thin films.

The nature of the observed difference was explained in [153]. We now analyze the average trajectory length L of an atomic particle that has passed through a film. Figure 12 shows the ratio of the average particle trajectory length L calculated in [153] to the target thickness d as a function of the bombarding proton energy. Data are presented for copper, silver, and gold targets. It is seen that, for energies on the order of 1 keV, the L/d ratio is approximately 2.5, and it tends to unity with increasing energy.

Thus, to determine the electronic stopping losses by the method of passing through, it is necessary to divide the energy loss value not by the film thickness but by the average trajectory length in the film.

Figure 13a shows the electronic stopping losses as a function of the incident particle energy for the H–Ag system. The dots are the experimental data, and the dashed line is the SRIM calculation data. It is evident from the figure that the data obtained by passing through differ significantly from those obtained by the reflection method. If the experimental data yielded by the analysis of thin films are adjusted for the L/d ratio, they coincide with the reflection data (Fig. 136).

Figure 13 also shows that in the low energy region the SRIM code yields incorrect values of the electronic stopping losses. The SRIM program uses the dependence $\mathrm{d}E/\mathrm{d}x \sim E^{0.5}$ (dashed curve in Fig. 13). Describing the adjusted data by a power law, we obtain $\mathrm{d}E/\mathrm{d}x = 2.08E^{0.68}$ for copper, $\mathrm{d}E/\mathrm{d}x = 1.56E^{0.81}$ for silver, and $\mathrm{d}E/\mathrm{d}x = 1.36E^{0.86}$ for gold (here, $\mathrm{d}E/\mathrm{d}x$ is measured in eV Å^{-1} units, and E in keV). Thus, at energies of less than 10 keV in the cases considered, the dependence of the electronic stopping losses differs from that predicted by generally accepted models. For the H–Au case, a theoretical calculation was made [154] which agrees with the adjusted data for $\mathrm{d}E/\mathrm{d}x$. According to the authors of [154], this difference is due to the simultaneous excitation of several electronic shells of the target atoms.

Thus, the differences among measurement data provided by different methods are associated with the interpretation of the results obtained. In computer modeling the passage of

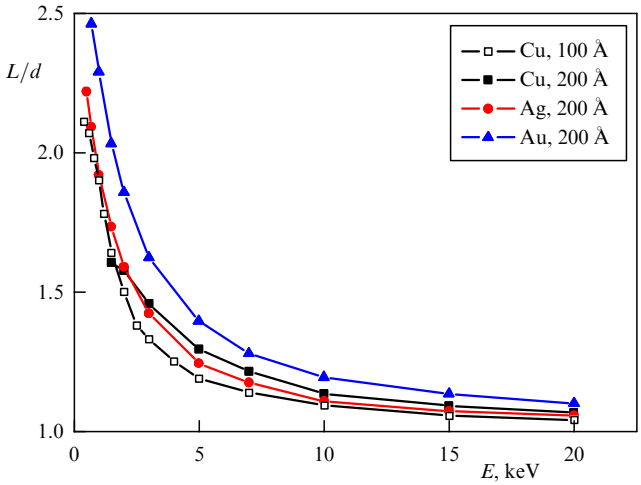

Figure 12. Ratio of average length of particle trajectory L to target thickness d as a function of bombarding proton energy. Data are presented for copper, silver, and gold targets.

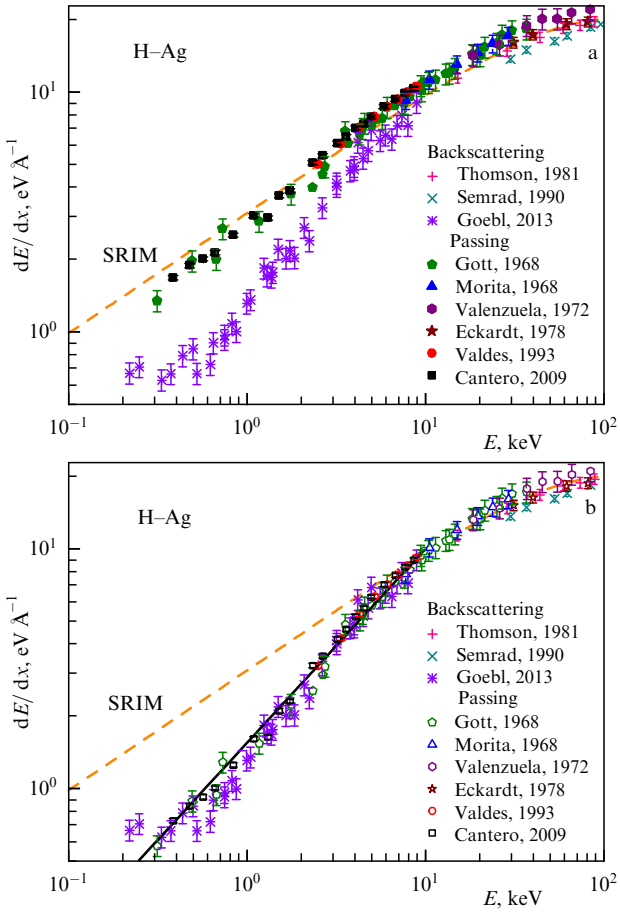

Figure 13. Electronic stopping losses as a function of incident particle energy in H–Ag system. Dots show experimental data from NDS database. Dashed line is SRIM calculation. (a) Data for passing configuration are not adjusted for L/d ratio. (b) Data for passing configuration are adjusted for L/d ratio.

particles through a substance, we recommend taking into account the correction for multiple scattering and using the parameter energy loss per unit trajectory length. It is also necessary to take into account the deviation in the dE/dx dependence on the proportionality of the velocity of the incident particle.

10. Effect of surface potential barrier on particle sputtering coefficients

Sputtering is used to etch the surface of solids, to clean surfaces of unwanted impurities, to obtain thin films, to determine surface composition, and in sputtering ion sources. A detailed review of solid sputtering studies is presented in [2–4, 6, 17].

In modeling sputtering, it is necessary to take into account the presence of a surface potential barrier. In calculations, the sublimation heat (energy) E_s is taken as the surface binding energy. The shape of the potential barrier at the solid–vacuum interface affects the calculation results. In most calculations made by Eckstein's group [5], a planar potential barrier is used. The planar potential barrier model is favored by the fact that the experimental energy spectra of sputtered particles exhibit a maximum [4]. If the solid–vacuum interface were an isotropic potential barrier, the maximum would be observed at zero energy, in disagreement with the experimental data. However, under conditions of strong wall sputtering in a tokamak reactor, the nature of the surface changes. As a limiting case, we considered a surface consisting of atomic-sized tips. In this case, a spherical potential barrier is applicable.

An important problem in operating thermonuclear installations is the durability of structural materials. It is affected by sputtering by neutral atoms emitted from the plasma. Beryllium and tungsten are proposed as the materials. Hydrogen isotopes will be the bombarding atoms.

Figure 14 shows data for a beryllium [155] and tungsten [156] target. It is seen that the experimental data for Be feature a large scatter, significantly exceeding the experimental errors (10–20%). In our opinion, this is due to the presence of contamination on the surface, oxides, and different surface roughness. In the case of W, the scatter of data is significantly smaller, and the experimental data are closer to the calculation for a planar barrier describing a smooth surface. The calculations of Eckstein's group [5, 157] lie between those for a smooth (planar barrier) and those for a rough (spherical barrier) surface.

In this case, sputtering of the surface layers by a flux of backscattered particles dominates. The Sigmund theory was modified for this case in [158, 159]. As can be seen from Fig. 14, the calculation using the Falcone formula [158, 159] agrees fairly well with the results of computer modeling for a planar potential barrier. For the H–Be system, the formula predicts the sputtering threshold quite well, while for the T–Be system the agreement is worse. The authors of [158] note that the Falcone formula yields good results for $M_1 \ll M_2$.

A comment is relevant regarding the sputtering threshold energy. The sputtering threshold energy E_{th} is the minimum energy of the incident ions at which sputtering is possible. The sputtering threshold energy cannot be obtained directly from

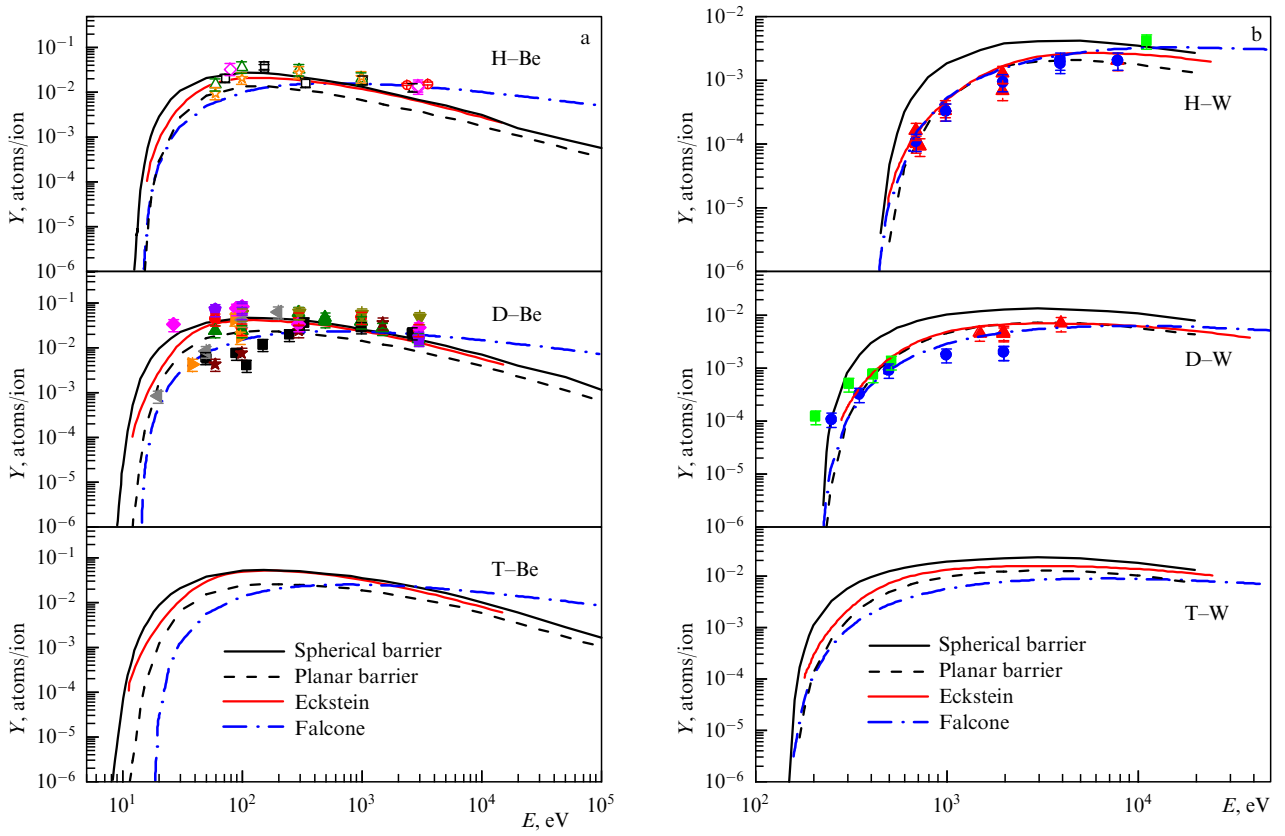

Figure 14. Dependence of sputtering coefficient of (a) beryllium and (b) tungsten on collision energy at normal incidence of a beam on a target for various isotopes. Calculations from studies [155, 156] for a spherical barrier — solid bold line; for a planar barrier — dashed bold line. Solid thin line shows calculation of Eckstein's group made using SDTrimSP program [5, 157]. Dashed thin line represents calculation based on Falcone formula [158, 159]. Dots show experimental data of various authors from monograph [5].

experiment. Usually, extrapolation of experimental or calculated data is applied. Eckstein and Preuss proposed the formula [160]

$$Y(E) = qs_n^{\mathrm{KrC}}(\varepsilon)\,\frac{(E/E_{\mathrm{th}}-1)^{\mu}}{(\lambda/\omega(\varepsilon))+(E/E_{\mathrm{th}}-1)^{\mu}} \qquad (10.1)$$

with nuclear stopping losses for the KrC potential:

$$s_{\mathrm{n}}^{\mathrm{KrC}}(\varepsilon) = \frac{0.5\ln(1+1.2288\varepsilon)}{\varepsilon+0.1728\sqrt{\varepsilon}+0.008\varepsilon^{0.1504}} = \frac{0.5\ln(1+1.2288\varepsilon)}{\omega(\varepsilon)}\,.$$

The reduced energy ε is represented as

$$\varepsilon = E\,\frac{M_2}{M_1+M_2}\,\frac{a_{\mathrm{L}}}{Z_1Z_2e^2}\,.$$

Lindhard's screening length is given by the formula

$$a_{\mathrm{L}} = \left(\frac{9\pi^2}{128}\right)^{1/3} a_{\mathrm{B}}\left(Z_1^{2/3}+Z_2^{2/3}\right)^{-1/2}, \quad a_{\mathrm{B}} = 0.529177\ \text{Å},$$

where a_{B} is the Bohr radius, and Z_1, Z_2 and M_1, M_2 are the atomic numbers and atomic masses of the projectile and target atoms, respectively. The threshold energy E_{th} and the values of q, λ, and μ are fitting parameters.

In [155], in studying threshold dependences, it was noted that near the threshold it is of importance to take into account the contribution of multiple scattering of bombarding particles.

As the presented results clearly show, the calculation methods provide fairly reliable values of the sputtering coefficients; however, a strong dependence on the surface condition is observed. In our opinion, the calculation results obtained should be linked to quantitative parameters characterizing the surface roughness, which could be determined experimentally. For a complex surface, for example, consisting of conical tips, it is of importance to develop the process of over-sputtering of the material, which can also affect the obtained results.

11. Effect of electronic stopping losses, surface potential barrier, and target structure on coefficient of particle reflection from surface

Reflection of ions by solid surfaces is a vast topic for experimental and theoretical research. The results of many years of studying the scattering of atomic particles by solid surfaces are presented in monographs [7–9, 161].

Scattering of ions by solid surfaces is successfully used to analyze the elemental composition of surfaces and films, and analytical methods of structural analysis are being developed. The most popular techniques of elemental analysis of the surface composition are Rutherford backscattering (RBS) and slow ion scattering spectroscopy (LEIS).

Knowledge of particle reflection coefficients is necessary to describe ion implantation processes. In the international thermonuclear reactor ITER, beryllium Be is chosen as the material of the first wall, and tungsten W is the material of the divertor. To predict the tokamak operation, it is necessary to know the coefficients of reflection R_{N} of hydrogen isotopes, helium, and various impurities from beryllium and tungsten.

Figure 15a displays the dependence of the reflection coefficient R_{N} on the bombarding particle energy [162] for a beryllium target and a number of projectiles. Figure 15a shows that, with an increase in the mass of the incident particle, the reflection coefficient drops sharply. As can be seen from Fig. 15, if the mass of the incident particle $M_1 \geqslant M_2$, where M_2 is the mass of the target atom, the reflection coefficient drops sharply, which is due to the absence of a contribution of single scattering to scattering at large angles.

Figure 15b presents the reflection coefficients [162] for a tungsten target and various projectiles. It is seen that the behavior of the reflection coefficient for the 'symmetric' W–W pair differs significantly from all other cases. The coefficient R_{N} is much smaller and drops sharply at energies on the order of 100 eV, which is also due to the absence of a contribution from single scattering.

Figure 16 separately presents the calculation of the reflection coefficient for the W–W system. The modeling was carried out for spherical and planar surface barriers. It is seen that, in the case of the planar barrier, the threshold energy for the dependence of the reflection coefficient on the collision energy is larger. The calculation for a smooth surface [162] agrees well with the modeling carried out by Eckstein's team [163].

Figure 16 displays the calculation of the sputtering coefficient Y for two models of the surface barrier. The reflection coefficients R_{N} are approximately 100 times smaller than the sputtering coefficients Y. If we normalize the curves, the thresholds for these processes virtually coincide.

For computer modeling of particle reflection from the surface of a solid, the model of electronic stopping losses underlying the calculation is essential. An analysis of the experimental data from the NDS database [117] shows that the electronic stopping losses do not coincide with the calculations of the widely used SRIM code [19] and require adjustment. Figure 17 shows the reflection coefficient as a function of the bombarding-particle energy for the H–W case. Calculation [162] for spherical and planar potential barriers is presented. For a smooth surface, the reflection coefficient drops sharply in the low-energy region. The simulation was carried out for the electronic stopping losses adjusted for the effect of multiple collisions for low energies (see Section 9). It is seen that the calculation for the adjusted stopping losses lies higher than that for the losses yielded by the SRIM code (Meluzova et al. [165]). For comparison, the calculation of Eckstein's team [164] is also displayed.

Figure 18 shows the reflection coefficients R_{N} depending on the energy of the incident particles for a crystalline and amorphous target for the He–W system. It is seen in Fig. 18 that the reflection coefficients for crystalline and amorphous targets differ. Due to the channeling effect in the crystalline target, the incident particles penetrate deeper into the target, and it is more difficult for them to escape; therefore, with increasing energy of the bombarding particles, the reflection coefficient sharply decreases. Good agreement with the experimental data [166] for the crystalline target is observed. Different codes give a similar dependence of R_{N} on E.

Unfortunately, reliable experimental data for the reflection coefficients of atomic particles are quite scant. Many data on ion scattering are available, and in most cases it is necessary to have data for all charge states, which can be obtained using the time-of-flight technique.

Computer modeling demonstrates the serious influence of electronic stopping losses, the surface potential barrier, and target structure on the coefficient of particle reflection

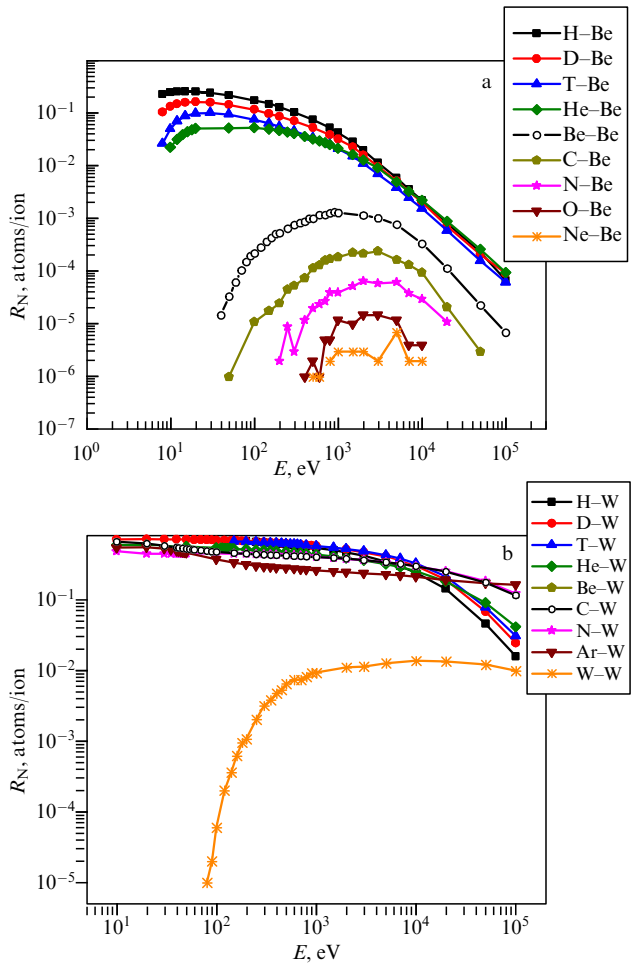

Figure 15. (a) Coefficients of particle reflection for a beryllium target as a function of energy for incident atoms H, D, T, He, Be, C, N, O, and Ne. For Be–Be system, calculation is presented for a planar potential barrier. (b) Coefficients of particle reflection for a tungsten target as a function of energy for incident atoms H, D, T, He, Be, C, N, Ar, and W. Data for W–W system are presented for a planar potential barrier. (Figures taken from [162].)

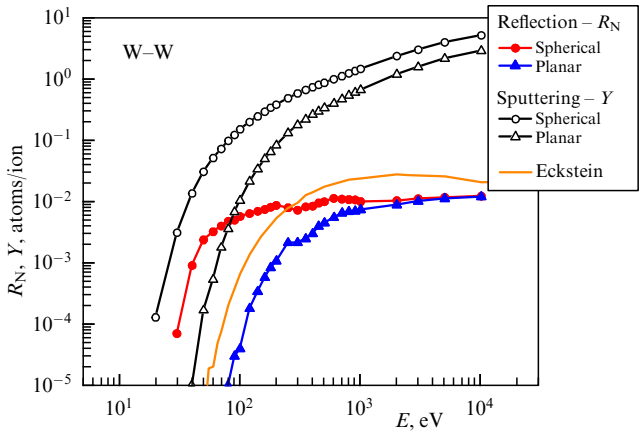

Figure 16. Comparison of reflection R_N and sputtering Y coefficients for W–W system [162]. Sputtering coefficients Y are shown by circles for a spherical surface barrier; open triangles, for a planar surface barrier. Reflection coefficients R_N are shown by red dots for a spherical surface barrier; filled triangles, for a planar surface barrier. Line shows calculation from [163] for a planar barrier.

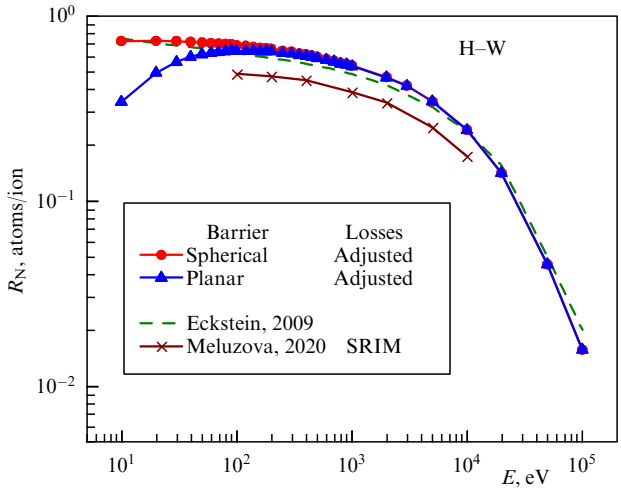

Figure 17. Reflection coefficients R_N for H–W system. Solid shapes (dots & triangles) — calculation [162] for energy losses adjusted for multiple collisions [153]. Dots — spherical barrier, triangles — planar barrier. Dashed curve — Eckstein calculation [164]. X's — calculation by Meluzova et al. from [165].

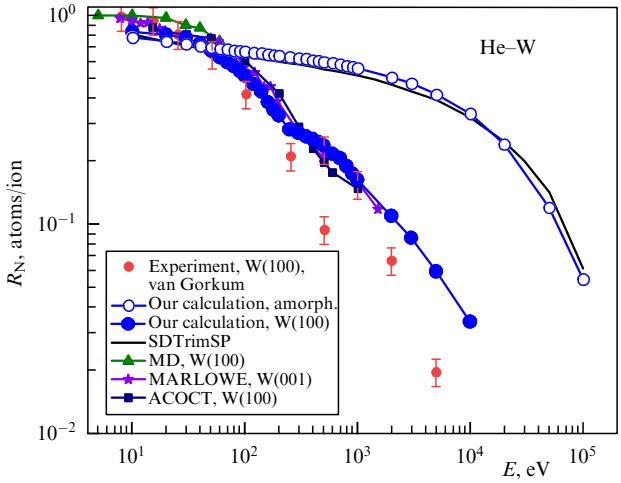

Figure 18. Reflection coefficients R_N as a function of incident particle energy for crystalline and amorphous targets for He–W system. Red dots — van Gorkum experiment [166]. Blue circles — calculation for amorphous target; blue dots — calculation for crystalline target W(100). Line — calculation using SDTrimSP program [164] for an amorphous target. Solid triangles show molecular dynamics calculations by Borovikov [167] for W(100) target. Asterisks are calculations made using MARLOWE program [168] for W(001) orientation. Squares show calculations made using ACOCT program (ACAT version for crystalline targets) [169] for W(100) orientation. (Figure taken from [162].)

from the surface. For further development of theoretical concepts, a significant extension of experimental studies is required with a mandatory analysis of the charge state of scattered particles.

12. Channeling of deuterium atoms in tungsten

One of the very interesting orientational effects in the study of ion scattering by crystals is the channeling effect: when the beam is oriented along open crystallographic directions, the particle ranges increase sharply. This effect was discovered by Robinson, Holmes, and Oen in 1963 [170] using computer simulation. Two years later, Lindhard developed the channel-

ing theory [171]. Tulinov made a significant contribution to the study of channeling and some other orientational effects [172]. Channeling studies and the areas of application of this effect are reviewed in [173].

We now consider the ranges of light ions in a heavy target using the D–W (100) system as an example. Figure 19 shows the depth distribution of the ranges, obtained using computer simulation [174], for incident atom energies ranging from 0.1 to 100 keV and normal incidence. It is seen that, starting from an energy of approximately 1 keV, the distribution splits into two components. A broad peak of particles scattered in the near-surface layers and a narrow peak at greater depths of particles captured in the channel are observed.

As the beam deviates from perpendicular incidence, the distribution is transformed, which corresponds to a decrease in the fraction of particles captured by the channel. At an inclination angle of 3°, the intensity of the channeling fraction decreases by a factor of more than 20. Formulas for the critical angle of axial channeling, i.e., the angle of capture of beam particles in the channel, were derived in [171]:

$$\psi_{\mathrm{L}}(E) \approx \left(\frac{3Z_1Z_2e^2a_{\mathrm{F}}^2}{d^3E}\right)^{1/4}, \quad E < \frac{2Z_1Z_2e^2d}{a_{\mathrm{F}}^2}, \qquad (12.1)$$

where Z_1 and Z_2 are the charge of the atomic nuclei of the particle and the target, respectively, $a_{\mathrm{F}} \approx 0.885a_{\mathrm{B}}(Z_1^{0.5} + Z_2^{0.5})^{-2/3}$ is the screening radius of the interatomic interaction, and a_{B} is the Bohr radius. The critical channeling angle for the D–W case at an initial energy of 100 keV is 3.3°.

Figure 20 displays the spatial distribution of particles captured in the channel for various depths of penetration into the target. To determine the spatial distribution of the channeling particles, only one channel was irradiated, marked in Fig. 20 by a square (depth $L = 1000$ Å). The beam incidence points were uniformly distributed over the square-shaped area. White spots show the positions of the target atoms. It is evident that a stable spatial structure is formed in the channel, which persists down to a depth of 9000 Å. With increasing depth, the atoms 'flow' into the neighboring channels.

In these figures, the colors indicate the 'concentration' values, i.e., the number of particles detected at each point in space, scaled by the largest number of detected particles (which corresponds to the value in the center of the channel

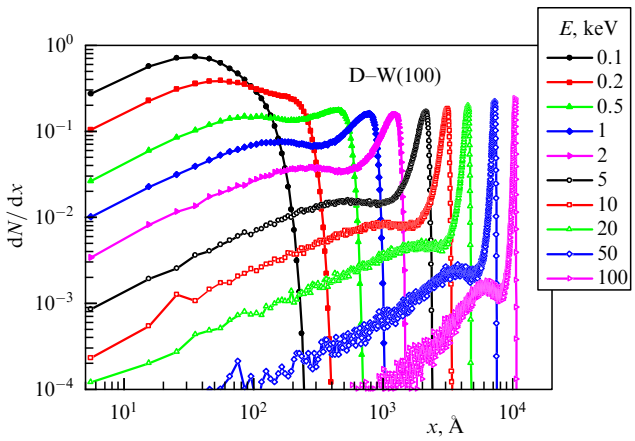

Figure 19. Distribution of ranges by depth for D–W(100); normal incidence. (Figure taken from [174].)

cross section). Also, for each case, there is a 3D representation of the concentration, which provides an additional visual description of the spatial distribution of ions inside the channel.

We now compare the resulting structure with that of the potential. According to Lindhard's theory, the behavior of particles in the channel is described by a continuous potential, which is the average value of the pair potential along the trajectory axis. To obtain the continuous potential, the Moliere potential was used, and, by varying the constants (c_1, c_2, c_3, d_1, d_2, d_3), agreement with the pair potential obtained by the DFT method was achieved. For the Moliere potential, the formula for the continuous potential can be represented as [175]

$$U(R) = \frac{2Z_1Z_2e^2}{d}\left[c_1K_0\left(d_1\frac{R}{a_{\mathrm{TF}}}\right) + c_2K_0\left(d_2\frac{R}{a_{\mathrm{TF}}}\right) + c_3K_0\left(d_3\frac{R}{a_{\mathrm{TF}}}\right)\right], \qquad (12.2)$$

where K_0 is the zero-order Bessel function of the second kind.

Figure 20 displays equipotential lines for the values of the continuous potential of 10, 20, and 50 eV for the depth $L = 3000$ Å. The circles in Fig. 20 label the regions where the channeled particles do not penetrate. On the boundaries of these regions, the value of the potential at the channel edge, $U(R_m)$, can be estimated yielding 10 eV. Note that

$$U(R_m) = E_\perp = E\sin^2\psi, \qquad (12.3)$$

where $E_\perp$ is the perpendicular component of the channeled-particle energy, and ψ is the maximum value of the trajectory deviation angle. The obtained values of $U(R_m)$ can be used to find the value $\psi = 0.57°$ for the D–W case, which is significantly less than the critical channeling angle. This implies that the beam of channeled particles is focused when moving through the crystal.

The observed pyramidal spatial structure is formed at the early stages of the ion path and remains qualitatively the same up to approximately 90% of the ion range in the crystal.

The formation of a stable spatial structure as a result of focusing in channeling can be used to experimentally determine the potential by studying the angular distribution of ions that have passed 30–60% of the range through the crystal under channeling conditions [176] and to analyze the topography of the surface layers of the film. Analysis of the energy spectrum allows us to determine the cross section of electronic stopping of channeled particles.

13. Conclusions

The use of computer modeling methods in combination with the analysis of experimental data makes it possible to significantly refine our understanding of the interaction of atomic particle beams with matter and to propose new experiments.

Equations (3.3) and (3.4) are presented for estimating the screening constant, obtained from first principles, which can be used for adjusting the scattering cross section when applying the Rutherford backscattering method and for estimating adjustments to the nuclear fusion cross section when carrying out measurements on targets containing electrons.

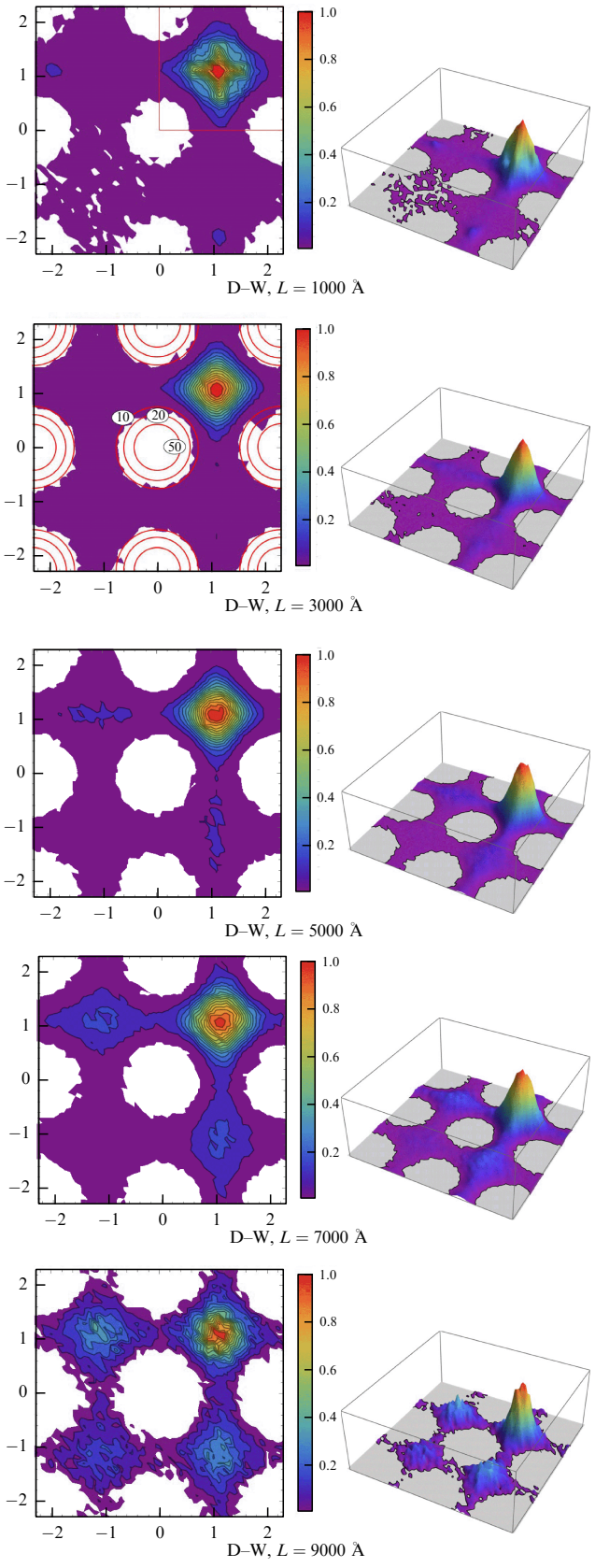

Figure 20. Spatial distribution of D atoms with an energy of 100 keV at various depths L in W(100). Distance (in Å) is shown on coordinate axes. Color scale shows the number of particles detected at each point in space divided by the largest number of particles detected for each figure. In first figure of the set, the region irradiated by D beam is indicated as a red square. Positions of lattice atoms correspond to centers of empty areas. Equipotential lines for continuous potential of 10 eV, 20 eV, and 50 eV are shown at a depth of L = 3000 Å. (Figure taken from [174].)

A formula for the Zinoviev potential (3.5) is given in [41], which makes it possible to rapidly assess the interaction potential. In choosing the interaction potential to describe particle trajectories, it is recommended to employ the calculation of the potential for specific systems using the density functional approximation [43, 46] and taking into account spectroscopic data on the potential well parameters [45].

In computer calculations, the Lindhard approximation is often used, in which nuclear and electronic stopping losses are considered in an additive way. A comparison with the experiment carried out in Section 4 shows that the accuracy of this approximation is 15–20%, depending on the range of energies considered. With the specified accuracy, the Lindhard curve for a specific potential, obtained using Eqn (4.6) and the parameters presented in the Table, can be used to calculate the elastic scattering cross section.

It was found that an adjustment should be introduced into the interaction potential for particle collisions with metals, taking into account the interaction with conduction electrons. Specific Eqns (5.5), (5.7), and (5.10) are presented, which take into account the screening of protons and hydrogen atoms when passing through metals. An example of using these formulas to estimate the passage of particles through thin films is given; they are recommended for use in calculating nuclear stopping losses [70].

NSP were calculated for 48 systems using the potential obtained in the DFT approximation with adjustment of the potential well parameters based on the results of spectroscopic measurements [46]. The calculation yields the same values of energy losses in both the classical and quasi-classical cases, provided condition $l \gg 1$ is satisfied.

An additional maximum in the NSP cross sections at low energies, associated with particle scattering on a potential well, should be taken into account. The presence of an additional peak in the NSP cross sections should be taken into account at collision energies of less than 100 eV; this is especially important when calculating the trajectories of recoil particles during sputtering.

A new mechanism for calculating electronic stopping losses is being considered, which makes a dominant contribution in collisions of particles of medium masses at keV energies. It is associated with the promotion of molecular orbitals during particle collisions and the formation of autoionization states.

Scaling is proposed to estimate ionization cross sections if K, L, M shells are excited. Examples of calculating stopping powers using measured cross sections for the Ar–Ar case and using scaling to calculate stopping losses for the Ne–Si case are given.

It is shown that quantitative agreement between the cross section of stopping losses and the sum of the contributions of ionization, excitation, and charge exchange can be achieved if significant losses of energy due to fast knocked-out electrons are taken into account. At high collision energies, up to 70% of the total stopping losses consists of the kinetic energy of emitted electrons. To estimate the electron energy at $v < 2$ at. units in the dynamic ionization approximation, Eqn (8.4) is proposed, which describes the experimental data well; at high energies, it is recommended to use the Born approximation (8.5).

When describing the passage of particles through matter, we recommend taking into account the correction due to multiple scattering and using the energy loss per unit trajectory length as the parameter. We also recommend

using experimental data obtained from the analysis of the spectrum of backscattered particles. The differences among measurement data provided by different methods is associated with the interpretation of the results obtained.

It is shown that the surface potential barrier, surface roughness, and target structure significantly affect sputtering and particle reflection from the surface; it is also important to correctly take ESP into account. An evaluation formula (10.1) for the sputtering coefficient is presented.

Application of the computer modeling demonstrates the significant influence of electronic stopping losses, the surface potential barrier, and target structure on the coefficient of particle reflection from the surface. It is concluded that, for the further development of theoretical concepts, a significant extension of experimental studies with mandatory analysis of the charge state of scattered particles is necessary.

In analyzing the channeling of deuterium atoms in crystalline tungsten W(100), channeling of atoms is shown to occur at relatively low energies of ~ 2 keV. At high energies, the beam is focused, and an experiment is proposed that allows testing the continuous potential model and the features of particle stopping when moving along the channel axis.

References

1. Avakyan S V et al. *Collision Processes and Excitation of UV Emission from Planetary Atmospheric Gases* (New York: Gordon and Breach, 1998); *Secheniya Protsessov Ionizatsii i Vozbuzhdeniya UF Izluchenuiya pri Stolknoveniyakh Elektronov, Ionov i Fotonov s Atomami i Molekulami Atmosfernykh Gazov* (Cross Sections of Ionization and Excitation of UV Radiation in Collisions of Electrons, Ions, and Photons with Molecules of Atmospheric Gases) (St. Petersburg: GOI, 2000)
2. Ryssel H, Ruge I *Ion Implantation* (Chichester: Wiley, 1986); Translated into Russian: *Ionnaya Implantatsiya* (Moscow: Nauka, 1983)
3. Behrisch R (Ed.) *Sputtering by Particle Bombardmen* Vol. 1 *Physical Sputtering of Single-Element Solids* (Topics in Applied Physics, Vol. 47) (Berlin: Springer-Verlag, 1981); Translated into Russian: *Raspylenie Tverdykh Tel Ionnoi Bombardirovkoi* Issue 1. *Fizicheskoe Raspylenie Odnoelementnykh Tverdykh Tel* (Moscow: Mir, 1984)
4. Behrisch R (Ed.) *Sputtering by Particle Bombardmen* Vol. 2 *Sputtering of Alloys and Compounds, Electron and Neutron Sputtering, Surface Topography* (Topics in Applied Physics, Vol. 52) (Berlin: Springer-Verlag, 1983); Translated into Russian: *Raspylenie Tverdykh Tel Ionnoi Bombardirovkoi* Issue 2. *Raspylenie Splavov i Soedinenii, Raspylenie pod Deistviem Elektronov i Neitronov, Rel'ef Poverkhnosti* (Moscow: Mir, 1986)
5. Behrisch R (Ed.) *Sputtering by Particle Bombardmen* Vol. 3 *Characteristics of Sputtered Particles, Technical Applications* (Topics in Applied Physics, Vol. 64) (Berlin: Springer-Verlag, 1991); Translated into Russian: *Raspylenie Tverdykh Tel Ionnoi Bombardirovkoi* Issue 3. *Kharakteristiki Raspylennykh Chastits, Primeneniya v Tekhnike* (Moscow: Mir, 1998)
6. Behrisch R, Eckstein W (Eds) *Sputtering by Particle Bombardment: Experiments and Computer Calculations from Threshold to MeV Energies* (Topics in Applied Physics, Vol. 110) (Berlin: Springer, 2007)
7. Sigmund P *Phys. Rev.* **184** 383 (1969)
8. Mashkova E S, Molchanov V A *Medium-energy Ion Reflection from Solids* (Amsterdam: North-Holland, 1985); Translated from Russian: *Rasseyanie Ionov Srednikh Energii Poverkhnostyami Tverdykh Tel* (Moscow: Atomizdat, 1980)
9. Parilis E S et al. *Teoriya Rasseyaniya Atomov Srednikh Energii Poverkhnost'yu Tverdogo Tela* (Theory of Reflection of Medium-energy Atoms by the Surface of a Solid Body) (Tashkent: FAN, 1987)
10. Kurnaev V A, Mashkova E S, Molchanov V A *Otrazhenie Legkikh Ionov ot Poverkhnosti Tverdogo Tela* (Reflection of Light Ions from the Surface of a Solid Body) (Moscow: Energoatomizdat, 1985)
11. Gott Yu V *Vzaimodeistvie Chastits s Veshchestvom v Plazmennykh Issledovaniyakh* (Particle-Matter Interactions in Plasma Research) (Moscow: Atomizdat, 1978)
12. Gott Yu V *Vzaimodeistvie Medlennykh Chastits s Veshchestvom i Diagnostika Plazmy* (Interaction of Slow Particles with Matter and Plasma Diagnostics) (Moscow: Atomizdat, 1973)
13. Ma B M *Nuclear Reactor Materials and Applications* (New York: Van Nostrand Reinhold Co., 1983); Translated into Russian: *Materialy Yadernykh Energeticheskikh Ustanovok* (Moscow: Energoatomizdat, 1987)
14. Hoffelner W *Materials for Nuclear Plants* (London: Springer, 2013)
15. Klenov G I, Khoroshkov V S *Phys. Usp.* **59** 807 (2016); *Usp. Fiz. Nauk* **186** 891 (2016)
16. Sigmund P *Particle Penetration and Radiation Effects* (London: Springer, 2014)
17. Pleshivtsev N V, Bazhin A I *Fizika Vozdeistviya Ionnykh Puchkov na Materialy* (Physics of the Effect of Ion Beams on Materials) (Moscow: Vuzovskaya Kniga, 1998)
18. Eckstein W *Computer Simulation of Ion-Solid Interactions* (Berlin: Springer, 1991); Translated into Russian: *Komp'yuternoe Modelirovanie Vzaimodeistviya Chastits s Poverkhnost'yu Tverdogo Tela* (Moscow: Mir, 1995)
19. SRIM - The Stopping and Range of Ions in Matter - code, http://srim.org/
20. Lindhard J, Scharff M *Phys. Rev.* **124** 128 (1961)
21. Robinson M T, Oen O S *Phys. Rev.* **132** 2385 (1963)
22. Mutzke A et al., SDTrimSP Version 6.00. IPP 2019-02 (Garching: IPP, 2019)
23. Biersack J P, Steinbauer E, Bauer P *Nucl. Instrum. Meth. Phys. Res. B* **61** 77 (1991)
24. Babenko P Yu, Zinoviev A N, Shergin A P *JETP Lett.* **101** 840 (2015); *Pis'ma Zh. Eksp. Teor. Fiz.* **101** 940 (2015)
25. Babenko P Yu et al. *J. Exp. Theor. Phys.* **128** 523 (2019); *Zh. Eksp. Teor. Fiz.* **155** 612 (2019)
26. Torrens I M *Interatomic Potentials* (New York: Academic Press, 1972)
27. Robinson M T, Torrens I M *Phys. Rev. B* **9** 5008 (1974)
28. Gaydaenko V I, Nikulin V K *Chem. Phys. Lett.* **7** 360 (1970)
29. Ziegler J F, Biersack J P, Littmark U *The Stopping and Range of Ions in Solids* Vol. 1 (New York: Pergamon Press, 1983)
30. Connor D J O, Biersack J E *Nucl. Instrum. Meth. Phys. Res. B* **15** 14 (1986)
31. Lane G H, Everhart E *Phys. Rev.* **120** 2064 (1960)
32. Afrosimov V V, Gordeev Yu S, Zinoviev A N *Sov. Phys. JETP* **39** 950 (1974); *Zh. Eksp. Teor. Fiz.* **66** 1933 (1974)
33. Firsov O B *Zh. Eksp. Teor. Fiz.* **24** 279 (1953)
34. Firsov O B *Sov. Phys. JETP* **6** 534 (1958); *Zh. Eksp. Teor. Fiz.* **33** 696 (1957)
35. Moliere G *Z. Naturforsch. A* **2** 133 (1949)
36. Jensen H *Z. Phys. B* **77** 722 (1932)
37. Wilson W D, Haggmark L G, Biersack J P *Phys. Rev. B* **15** 2458 (1977)
38. Zinoviev A N *Nucl. Instrum. Meth. Phys. Res. B* **406** 465 (2017)
39. Zinoviev A N *J. Surf. Invest. X-Ray, Synchrotron Neutron Tech.* **12** 554 (2018); *Poverkhnost'. Rentgen. Sinkhrotron. Neitron. Issled.* (6) 43 (2018)
40. Lu C C et al. *At. Data Nucl. Data Tables* **3** 1 (1971)
41. Zinoviev A N *Tech. Phys.* **53** 13 (2008); *Zh. Tekh. Fiz.* **78** 15 (2008)
42. Norlund K, Runeberg N, Sundholm D *Nucl. Instrum. Meth. Phys. Res. B* **132** 45 (1997)
43. Zinoviev A N, Norlund K *Nucl. Instrum. Meth. Phys. Res. B* **406** 511 (2017)
44. Meluzova D S et al. *Nucl. Instrum. Meth. Phys. Res. B* **460** 4 (2019)
45. Luo Y-R *Comprehensive Handbook of Chemical Bond Energies* (Boca Raton, FL: CRC Press, 2007)
46. Zinoviev A N, Babenko P Yu, Nordlund K *Nucl. Instrum. Meth. Phys. Res. B* **508** 10 (2021)
47. Bjorkas C et al. *J. Phys. Condens. Matter* **21** 445002 (2009)
48. Prokof'ev M V, Svetukhin V V, Tikhonchev M Yu *Izv. Samarsk. Nauch. Tsentra Ross. Akad. Nauk* **15** 1024 (2013)
49. Granberg F, Byggmästar J, Nordlund K *J. Nucl. Mater.* **556** 153158 (2021)
50. Bjorkas C, Nordlund K *J. Nucl. Mater.* **439** 174 (2013)

51. Lyashenko A et al. *J. Nucl. Mater.* **542** 152465 (2020)
52. Tersoff J *Phys. Rev. B* **37** 6991 (1988)
53. Rapaport D C *The Art of Molecular Dynamics Simulation* (Cambridge: Cambridge Univ. Press, 2004)
54. Lindhard J, Nielsen V, Scharff M *Mat.-Fys. Medd. Dan. Vid. Selsk.* **36** (10) 1 (1968)
55. Winterbon K B *Rad. Eff.* **13** 215 (1972)
56. Littmark U, Ziegler J F *Phys. Rev. A* **23** 64 (1981)
57. Babenko P Yu, Zinoviev A N *Tech. Phys.* **69** 1886 (2024); *Zh. Tekh. Fiz.* **93** 1272 (2023)
58. Hartung H et al. *Phys. Lett. A* **119** 457 (1987)
59. Hartung H et al. *J. Phys. B* **18** L433 (1985)
60. Gartker K, Hehl K *Phys. Status Solidi B* **94** 231 (1979)
61. Loftager P et al. *Phys. Rev. A* **20** 1443 (1979)
62. Loftager P, Claussen G, in *ICPEAC VI* (Cambridge, USA, 1969) p. 518
63. Bruckner B et al. *Nucl. Instrum. Meth. Phys. Res. B* **470** 21 (2020)
64. Shulga V I *Rad. Eff.* **100** 71 (1986)
65. Babenko P Yu et al. *Tech. Phys. Lett.* **48** 50 (2022); *Pis'ma Zh. Tekh. Fiz.* **48** 10 (2022)
66. Verbeek H, Eckstein W, Bhattacharya R S *J. Appl. Phys.* **51** 1783 (1980)
67. Babenko P Yu, Zinoviev A N, Tensin D S *Tech. Phys.* **67** 1416 (2022); *Zh. Tekh. Fiz.* **92** 1643 (2022)
68. Fama M et al. *Nucl. Instrum. Meth. Phys. Res. B* **164** 241 (2000)
69. Archubi C et al. *Phys. Status Solidi B* **241** 2389 (2004)
70. Babenko P Yu, Mikhailov V S, Zinoviev A N *JETP Lett.* **117** 725 (2023); *Pis'ma Zh. Eksp. Teor. Fiz.* **117** 723 (2023)
71. Dedkov G V *Phys. Usp.* **38** 877 (1995); *Usp. Fiz. Nauk* **165** 919 (1995)
72. Saitoh K *Rad. Eff.* **82** 205 (1984)
73. Kittel C *Introduction to Solid State Physics* 8th ed. (New York: John Wiley and Sons, 2005)
74. Landau L D, Lifshitz E M *Quantum Mechanics*: *Non-Relativistic Theory* (Oxford: Pergamon Press, 1977); Translated from Russian: *Kvantovaya Mekhanika* (*Nerelyativistskaya Teoriya*) (Moscow: Fizmatlit, 2004)
75. Mott N F, Massey H S W *Theory of Atomic Collisions* (Oxford: Oxford Univ. Press, 1965); Translated into Russian: *Teoriya Atomnykh Stolknovenii* (Moscow: Mir, 1969)
76. Bethe H A *Ann. Physik* **5** 325 (1930)
77. Bloch F *Ann. Physik* **16** 285 (1933)
78. Fermi E, Teller E *Phys. Rev.* **72** 399 (1947)
79. Andersen H H, Ziegler J F *Hydrogen Stopping Powers and Ranges in All Elements. The Stopping and Range of Ions in Matter* Vol. 3 (New York: Pergamon Press, 1977)
80. Fink D et al. *Nucl. Instrum. Meth.* **218** 171 (1983)
81. Fink D *Nucl. Instrum. Meth.* **218** 817 (1983)
82. Firsov O B *Sov. Phys. JETP* **9** 1076 (1959); *Zh. Eksp. Teor. Fiz.* **36** 1517 (1959)
83. Oen O S, Robinson M T *Nucl. Instrum. Meth.* **132** 647 (1976)
84. Akhiezer I A, Davydov L N *Sov. Phys. Usp.* **22** 804 (1979); *Usp. Fiz. Nauk* **129** 239 (1979)
85. Sigmund P *Nucl. Instrum. Meth. Phys. Res. B* **406** 391 (2017)
86. Montanari C C, Miraglia J E *Phys. Rev. A* **96** 012707 (2017)
87. Zinoviev A N, Babenko P Yu, Meluzova D S, Shergin A P *JETP Lett.* **108** 633 (2018); *Pis'ma Zh. Eksp. Teor. Fiz.* **108** 666 (2018)
88. Zinoviev A N, Babenko P Yu, Meluzova D S, Shergin A P *Nucl. Instrum. Meth. Phys. Res. B* **467** 140 (2020)
89. Duvenbeck A et al. *Phys. Rev. B* **77** 245444 (2008)
90. Fuls E N et al. *Phys. Rev.* **107** 704 (1957)
91. Kessel Q C, Everhart E *Phys. Rev.* **146** 16 (1966)
92. Bierman D J, Turkenburg W C *Physica* **67** 533 (1973)
93. Morgan G H, Everhart E *Phys. Rev.* **128** 667 (1962)
94. Kessel Q C, Rose P H, Grodzins L *Phys. Rev. Lett.* **22** 1031 (1969)
95. Zinoviev A N, Babenko P Yu, Shergin A P *J. Exp. Theor. Phys.* **163** 662 (2023); *Zh. Eksp. Teor. Fiz.* **163** 744 (2023)
96. Amme R C, Haugsjaa P O *Phys. Rev.* **177** 230 (1969)
97. Gilbody H B, Hasted J B *Proc. R. Soc. London A* **238** 334 (1957)
98. Cacak R K, Kessel Q C, Rudd M E *Phys. Rev. A* **2** 1327 (1970)
99. Meskhi G G "Osobennosti radiatsionnogo i Ozhe-raspada vnutrennikh vakansii, obrazuyushchikhsya v atomnykh stolknoveniyakh" ("Features of radiation and Auger decay of internal vacancies formed in atomic collisions"), Candidate's Dissertation in Phys. and Math. (Leningrad: Ioffe Physical-Technical Institute, 1983)
100. Echenique P M, Flores F, Ritchie R H *Solid State Phys.* **43** 229 (1990)
101. Grahmann G, Kalbitzer S *Nucl. Instrum. Meth. Phys. Res. B* **132** 119 (1976)
102. Zinoviev A N, Babenko P Yu, Shergin A P *J. Surf. Invest. X-Ray, Synchrotron Neutron Tech.* **14** 1304 (2020); *Poverkhnost'. Rentgen, Sinkhrotron. Neitron. Issled.* (12) 64 (2020)
103. Babenko P Yu, Zinoviev A N, Shergin A P *Nucl. Instrum. Meth. Phys. Res. B* **354** 142 (2015)
104. Briggs J S, Macek J *J. Phys. B* **5** 579 (1972)
105. Zinoviev A N, Babenko P Yu, Shergin A P *JETP Lett.* **114** 18 (2021); *Pis'ma Zh. Eksp. Teor. Fiz.* **114** 13 (2021)
106. Meyerhof W E, Taulbjerg K *Annu. Rev. Nucl. Sci.* **27** 279 (1977)
107. Lennard W N, Mitchell I V, Forster J S *Phys. Rev. A* **18** 1949 (1978)
108. Foster C et al. *J. Phys. B* **9** 1943 (1976)
109. Zinoviev A N, Ovchinnikov S Yu, Gordeev Yu S *Sov. Tech. Phys. Lett.* **7** 139 (1981); *Pis'ma Zh. Tekh. Fiz.* **7** 139 (1981)
110. Ovchinnikov S Yu, Solov'ev E A *JETP Lett.* **64** 280 (1986); *Pis'ma Zh. Eksp. Teor. Fiz.* **91** 477 (1986)
111. Ogurtsov G N et al. *Phys. Rev. A* **53** 2391 (1996)
112. Pieksma M, Ovchinnikov S Yu *J. Phys. B* **24** 2699 (1991)
113. Stolterfoht N *Phys. Rev. A* **12** 1313 (1975)
114. Zinoviev A N, Babenko P Yu *J. Surf. Invest. X-Ray, Synchrotron Neutron Tech.* **15** 623 (2021); *Poverkhnost'. Rentgen, Sinkhrotron. Neitron. Issled.* (6) 94 (2021)
115. Zinoviev A N, Babenko P Yu *Nucl. Instrum. Meth. Phys. Res. B* **536** 82 (2023)
116. ALADDIN database, https://www-amdis.iaea.org/ALADDIN/
117. NDS database, https://www-nds.iaea.org/stopping/
118. Cabrera-Trujillo R et al. *Phys. Rev. Lett.* **84** 5300 (2000)
119. Kirchner T, Horbatsch M, Ludde H J *Phys. Rev. A* **66** 052719 (2002)
120. Schiwietz G, Grande P L *Phys. Rev. A* **84** 052703 (2011)
121. Chowdhury M R e al. *Phys. Rev. A* **102** 012819 (2020)
122. Commisso M et al. *Nucl. Instrum. Meth. Phys. Res. B* **256** 474 (2007)
123. Gassert H et al. *Phys. Rev. Lett.* **116** 073201 (2016)
124. Gravielle M S, Miraglia J E *Phys. Rev. A* **65** 022901 (2002)
125. Hasan A et al. *Phys. Rev. A* **74** 032703 (2006)
126. Kim H-K et al. *Phys. Rev. A* **85** 022707 (2012)
127. McSherry D M et al. *AIP Conf. Proc.* **576** 168 (2001)
128. Schultz D R et al. *Phys. Rev. A* **65** 052722 (2002)
129. Sigmund P, Glazov L G *Eur. Phys. J. D* **23** 211 (2003)
130. Rudd M E, Toburen L H, Stolterfoht N *At. Data Nucl. Data Tables* **18** 413 (1976)
131. Rudd M E, Toburen L H, Stolterfoht N *At. Data Nucl. Data Tables* **23** 405 (1979)
132. Moro M V et al. *Nucl. Instrum. Meth. Phys. Res. B* **498** 1 (2021)
133. Mery M et al. *Rad. Eff. Def. Solids* **176** 73 (2021)
134. Fama M et al. *Nucl. Instrum. Meth. Phys. Res. B* **193** 91 (2002)
135. Tran T T et al. *Phys. Rev. A* **100** 032705 (2019)
136. Konac G et al. *Nucl. Instrum. Meth. Phys. Res. B* **136** 159 (1998)
137. Moller S P et al. *Phys. Rev. Lett.* **88** 193201 (2002)
138. Andersen H H *Nucl. Instrum. Meth. Phys. Res. B* **194** 217 (2002)
139. Bruckner B *Nucl. Instrum. Meth. Phys. Res. B* **423** 82 (2018)
140. Cantero E D et al. *Phys. Rev. A* **80** 032904 (2009)
141. Valdes J E et al. *Phys. Rev. A* **49** 1083 (1994)
142. Markin S N et al. *Phys. Rev. B* **80** 205105 (2009)
143. Martínez-Tamayo G et al. *Phys. Rev. A* **51** 2285 (1995)
144. Goebl D et al. *Phys. Rev. A* **90** 042706 (2014)
145. Valdés J E et al. *Nucl. Instrum. Meth. Phys. Res. B* **73** 313 (1993)
146. Goebl D, Roth D, Bauer P *Phys. Rev. A* **87** 062903 (2013)
147. Valdés J E et al. *Nucl. Instrum. Meth. Phys. Res. B* **164** 268 (2000)
148. Blume R, Eckstein W, Verbeek H *Nucl. Instrum. Meth.* **168** 57 (1980)
149. Markin S N e al. *Phys. Rev. B* **78** 195122 (2008)
150. Paul H, Schinner A *Phys. Scripta* **69** C41 (2004)
151. Sigmund P, Schinner A *Nucl. Instrum. Meth. Phys. Res. B* **410** 78 (2017)
152. Goebl D et al. *Phys. Rev. A* **88** 032901 (2013)
153. Zinoviev A N, Babenko P Yu *JETP Lett.* **115** 560 (2022); *Pis'ma Zh. Eksp. Teor. Fiz.* **115** 603 (2022)
154. Zeb M A et al. *Phys. Rev. Lett.* **108** 225504 (2012)

155. Babenko P Yu, Mikhailov V S, Shergin A P, Zinoviev A N *Tech. Phys.* **68** 662 (2023); *Zh. Tekh. Fiz.* **93** 709 (2023)
156. Mikhailov V S, Babenko P Yu, Shergin A P, Zinoviev A N *J. Exp. Theor. Phys.* **137** 413 (2023); *Zh. Eksp. Teor. Fiz.* **164** 478 (2023)
157. Clark R E H *Atomic and Plasma-Material Interaction Data for Fusion* Vol. 7, Pt. B (Vienna: IAEA, 2001)
158. Falcone G, Gullo F *Phys. Lett. A* **125** 432 (1987)
159. Falcone G *Rivista Nuovo Cimento* **13** 1 (1990); Translated into Russian: *Usp. Fiz. Nauk* **162** 71 (1992)
160. Eckstein W, Preuss R *J. Nucl. Mater.* **320** 209 (2003)
161. Mashkova E S, Molchanov V A *Primenenie Rasseyaniya Ionov dlya Analiza Tverdykh Tel* (Application of Ion Scattering to Solid State Analysis) (Moscow: Energoatomizdat, 1995)
162. Mikhailov V S, Babenko P Yu, Shergin A P, Zinoviev A N *Tech. Phys.* **68** 1425 (2023) https://journals.ioffe.ru/articles/57492; *Zh. Tekh. Fiz.* **93** 1533 (2023) https://doi.org/10.61011/JTF.2023.11.56484.192-23
163. Eckstein W "Calculated sputtering, reflection and range values," IPP-9-132 (Garching: IPP, 2002)
164. Eckstein W "Reflection (Backscattering)," IPP-17-12 (Garching: IPP, 2009)
165. Meluzova D S, Babenko P Yu, Shergin A P, Zinoviev A N *J. Surf. Investig.* **14** 738 (2020); *Poverkhnost'. Rentgen., Sinkhrotron. Neitron. Issled.* (7) 98 (2020)
166. van Gorkum A A, Kornelsen E V *Rad. Eff.* **52** 25 (1980)
167. Borovikov V, Voter A F, Tang X-Z *J. Nucl. Mater.* **447** 254 (2014)
168. Robinson M T *J. Nucl. Mater.* **103** 525 (1981)
169. Yamamura Y *Nucl. Instrum. Meth. Phys. Res. B* **33** 429 (1988)
170. Robinson M T, Oen O S *Appl. Phys. Lett.* **2** 30 (1963)
171. Lindhard J *Mat.-Fys. Medd. Dan. Vid. Selsk.* **34** 1 (1965)
172. Tulinov A F *Sov. Phys. Usp.* **8** 864 (1966); *Usp. Fiz. Nauk* **87** 585 (1965)
173. Vantomme A *Nucl. Instrum. Meth. Phys. Res. B* **371** 12 (2016)
174. Tensin D S et al. *Nucl. Instrum. Meth. Phys. Res. B* **540** 33 (2023)
175. Ohtsuki Y-H *Charged Beam Interaction with Solids* (London: Taylor and Francis, 1983); Translated into Russian: *Vzaimodeistvie Zaryazhennykh Chastits s Tverdymi Telami* (Moscow: Mir, 1985)
176. Meluzova D S, Babenko P Yu, Shergin A P, Zinoviev A N *Tech. Phys. Lett.* **46** 235 (2020); *Pis'ma Zh. Tekh. Fiz.* **46** (5) 34 (2020)